RESONANCE BIFURCATIONS OF ROBUST HETEROCLINIC NETWORKS*

VIVIEN KIRK† CLAIRE POSTLETHWAITE‡ AND ALASTAIR M. RUCKLIDGE§

Abstract. Robust heteroclinic cycles are known to change stability in resonance bifurcations, which occur when an algebraic condition on the eigenvalues of the system is satisfied and which typically result in the creation or destruction of a long-period periodic orbit. Resonance bifurcations for heteroclinic networks are potentially more complicated because different subcycles in the network can undergo resonance at different parameter values, but have, until now, not been systematically studied. In this article we present the first investigation of resonance bifurcations in heteroclinic networks. Specifically, we study two heteroclinic networks in $\mathbb{R}^4$ and consider the dynamics that occurs as various subcycles in each network change stability. The two cases are distinguished by whether or not one of the equilibria in the network has real or complex contracting eigenvalues. We construct two-dimensional Poincaré return maps and use these to investigate the dynamics of trajectories near the network; a complicating feature of the analysis is that at least one equilibrium solution in each network has a two-dimensional unstable manifold. We use the technique developed in [18] to keep track of all trajectories within these two-dimensional unstable manifolds. In the case with real eigenvalues, we show that the asymptotically stable network loses stability first when one of two distinguished cycles in the network goes through resonance and two or six periodic orbits appear. In some circumstances, asymptotically stable periodic orbits can bifurcate from the network even though the subcycle from which they bifurcate is never asymptotically stable. In the complex case, we show that an infinite number of stable and unstable periodic orbits are created at resonance, and these may coexist with a chaotic attractor. In both cases, we show that near to the parameter values where individual cycles go through resonance, the periodic orbits created in the different resonances do not interact, i.e., the periodic orbits created in the resonance of one cycle are not involved in the resonance of the other cycle. However, there is a further resonance, for which the eigenvalue combination is a property of the entire network, after which the periodic orbits which originated from the individual resonances may interact. We illustrate some of our results with a numerical example.

Key words. heteroclinic cycle, heteroclinic network, resonance, resonance bifurcation

AMS subject classifications. 37C29, 37C40, 37C80

1. Introduction.

Heteroclinic cycles and networks are flow invariant sets that can occur robustly in dynamical systems with symmetry, and are frequently associated with intermittent behaviour in such systems. Various definitions of heteroclinic cycles and networks have been given in the literature; for examples, see [5,17,19,20,24]. We use the following definitions from [18]. For a finite-dimensional system of ordinary differential equations (ODEs), we define:

Definition. A *heteroclinic cycle* is a finite collection of equilibria $\{\xi_1,\dots,\xi_n\}$ of the ODEs, together with a set of heteroclinic connections $\{\gamma_1(t),\dots,\gamma_n(t)\}$, where $\gamma_j(t)$ is a solution of the ODEs such that $\gamma_j(t)\to\xi_j$ as $t\to-\infty$ and $\gamma_j(t)\to\xi_{j+1}$ as $t\to\infty$, and where $\xi_{n+1}\equiv\xi_1$.

*This work was supported by the EPSRC grant EP/G052603/1.

Definition. Let $\mathcal{C}_1, \mathcal{C}_2, \ldots$ be a collection of two or more heteroclinic cycles. We say that $\mathcal{N} = \bigcup_i \mathcal{C}_i$ forms a *heteroclinic network* if for each pair of equilibria in the network, there is a sequence of heteroclinic connections joining the equilibria. That is, for any pair of equilibria $\xi_j, \xi_k \in \mathcal{N}$, we can find a sequence of heteroclinic connections $\{\gamma_{p_1}(t), \ldots, \gamma_{p_l}(t)\} \in \mathcal{N}$ and a sequence of equilibria $\{\xi_{m_1}, \ldots, \xi_{m_{l+1}}\} \in \mathcal{N}$ such that $\xi_{m_1} \equiv \xi_j$, $\xi_{m_{l+1}} \equiv \xi_k$ and γ_{p_i} is a heteroclinic connection between ξ_{m_i} and $\xi_{m_{i+1}}$.

More generally, the heteroclinic orbits in a heteroclinic cycle may connect flow invariant sets other than equilibria (e.g., periodic orbits or chaotic saddles) but we will not consider such possibilities in this article. Our definition of a heteroclinic network does not require that there be an infinite number of heteroclinic cycles in a network, but in the networks we consider, (at least) one of the equilibria in the network has a two-dimensional unstable manifold and associated with this is an infinite number of heteroclinic connections between that equilibrium and another. We only consider the case that the set of equilibria in the network is finite.

Methods for determining the stability properties of an isolated heteroclinic cycle involving equilibria or periodic orbits are well-established [11, 19, 21–23, 26, 27], and their implementation is generally straightforward, at least in principle, because there is only one route around the cycle. In the most widely studied examples, all equilibria have one-dimensional unstable manifolds, and within these manifolds, the next equilibrium point in the cycle is a sink. One way a heteroclinic cycle can lose stability is in a resonance bifurcation. A resonance bifurcation is a global phenomenon, which occurs when an algebraic condition on the eigenvalues of the equilibria in the cycle is satisfied. Generically, resonance bifurcations are accompanied by the birth or death of a long-period periodic orbit. If the bifurcation occurs supercritically, then in the simplest case, the bifurcating periodic orbit is asymptotically stable and the heteroclinic cycle changes from being asymptotically stable to having a basin of attraction with measure zero. Resonance bifurcations from asymptotically stable heteroclinic cycles have been extensively studied; see [12, 22, 26, 27], for cases in which all eigenvalues are real, and [25] for a case with complex eigenvalues. Much less is known about resonance bifurcations of non-asymptotically stable cycles.

Stability of robust heteroclinic networks is less well understood. Some results are known (e.g., [3, 6–10, 13, 16–18, 20, 24]) but these are, in general, partial results and confined to specific examples. One source of difficulty is that there may be many different routes by which an orbit can traverse a heteroclinic network, and keeping track of all possibilities in the stability calculations can be challenging, particularly when one or more of the equilibria in the network has a two-dimensional unstable manifold. When this occurs, trajectories may go straight to an equilibrium point that is a sink within the unstable manifold, or may visit a saddle equilibrium point before moving on to the sink. A full analysis needs to account for all possibilities. In [18], we showed that it is possible to do this and so to establish relatively complete stability results for a specific class of problems in which all cycles in the network share

a common heteroclinic connection, despite there being several equilibria with two-dimensional unstable manifolds. In this case, we were able to derive conditions that determine the attractivity properties of the network. These conditions are network analogues of stability conditions for single heteroclinic cycles, and involve inequalities on combinations of the eigenvalues of the equilibria. By analogy with resonance bifurcations of heteroclinic cycles, we call the transition that occurs when one or more of the inequalities is reversed a resonance of a heteroclinic network.

In [18] it was noted that complicated dynamics could be associated with resonance in the network studied. Our aim in this article is to complete this analysis, and extend it to a closely related heteroclinic network (which is the same as that studied in [17], although in that article, no attempt was made to keep track of all trajectories in the two-dimensional unstable manifolds). We will then investigate resonance bifurcations in both networks in detail. We believe this is the first article to analyze network resonance in a systematic way.

Both networks have the basic structure shown schematically in figure 1.1. Specifically, each network consists of six equilibria, which we call A, B, X, Y, P and Q, and their symmetric copies, $-A$, $-B$, $-X$, $-Y$, $-P$, and $-Q$, along with a collection of heteroclinic connections between equilibria. The equilibria A and B are connected by a single (one-dimensional) heteroclinic connection from A to B. Equilibrium B has a two-dimensional unstable manifold associated with two different positive real eigenvalues, and there is a continuum of heteroclinic orbits lying within this manifold and connecting B to X, Y, P, Q, and their symmetric copies: there is a single connection from B to P and from B to Q, but an uncountable family of connections from B to X and from B to Y. The equilibria X and Y have one-dimensional unstable manifolds which are heteroclinic connections to A and $-A$. P and Q have two-dimensional unstable manifolds consisting of single heteroclinic connections to X and Y (and their symmetric copies) and continua of heteroclinic connections to A and $-A$.

The feature that distinguishes our two networks from one another is whether or not the Jacobian matrix of the flow evaluated at A has complex eigenvalues. In Case I, there are only real eigenvalues at A, while in Case II, A has a complex conjugate pair of eigenvalues with negative real part. Further details about the networks are given in Section 2.

We analyse the networks by deriving local and global maps that approximate the dynamics near and between the different equilibria in the network. This analysis is complicated by the fact that, for reasons explained in detail later, it is not always possible to write these maps explicitly. However, under certain approximations and assumptions about the dynamics near the networks, we are able to compose the maps; these approximations and assumptions mildly restrict the validity of our results. This then gives us information about the dynamics of all possible trajectories as they traverse the network and return close to where they started. The derivations of the maps, approximations and compositions are contained in sections 3 and 4.

Using the return maps, we are then, in section 5, able to determine existence criteria for fixed points of the maps, which correspond to periodic orbits in the original flow. These periodic orbits appear when resonance conditions for the network are broken. In the case of an asymptotically stable network losing stability, we find that the first conditions to be violated are those associated with one or the other of the subcycles within the network, that is, the conditions on the eigenvalues are the same as for a single cycle. In the network with real eigenvalues, either two or six periodic orbits appear at this initial resonance (including all symmetric copies). We also show that an asymptotically stable periodic orbit can bifurcate from a non-asymptotically stable heteroclinic cycle in this network. In the network with complex eigenvalues, we find that infinitely many periodic orbits appear at resonance. For both networks, if we remain in parameter space close to the point where the resonances of individual subcycles occur (we consider the eigenvalues of the equilibria as parameters), then the periodic orbits arising from the bifurcations of the subcycles do not interact, i.e., the periodic orbits created in the resonance of one cycle are not involved in the resonance of the other cycle. However, we find that there is a further resonance, for which the eigenvalue combination is a property of the entire network, after which the periodic orbits which originated from the individual resonances may interact, for instance when orbits arising from different resonances come together in saddle-node bifurcations.

In addition to bifurcating periodic orbits, we also find that a chaotic attractor may be created at a resonance bifurcation of the network with complex eigenvalues. This is detailed in section 5.2.4. Section 5.2.5 contains a numerical example showing both periodic orbits and a chaotic attractor.

In section 6 we look at resonance bifurcations of an isolated heteroclinic cycle with complex eigenvalues. When this cycle goes through resonance, infinitely many periodic orbits appear, in a similar manner to that seen within the network with complex eigenvalues. The analysis of this cycle allows us to conjecture which features of the dynamics of our Case II network arise from the existence of complex eigenvalues and which are a result of the network structure.

Section 7 concludes with discussion and avenues for further work.

2. The heteroclinic networks. We consider a system of ordinary differential equations, $\dot{\mathbf{x}} = \mathbf{f}(\mathbf{x})$, where $\mathbf{x} = (x_1, x_2, x_3, y_3) \in \mathbb{R}^4$ and $\mathbf{f} : \mathbb{R}^4 \to \mathbb{R}^4$ is a $\mathbf{C}^1$ vector-valued function. For both networks we consider, we assume this system has the following equivariance properties:

$$\kappa_i(\mathbf{f}(\mathbf{x})) = \mathbf{f}(\kappa_i(\mathbf{x})), \qquad i = 1, 2,$$

where

$$\kappa_1 : (x_1, x_2, x_3, y_3) \to (-x_1, x_2, x_3, y_3), \tag{2.1}$$

$$\kappa_2 : (x_1, x_2, x_3, y_3) \to (x_1, -x_2, x_3, y_3). \tag{2.2}$$

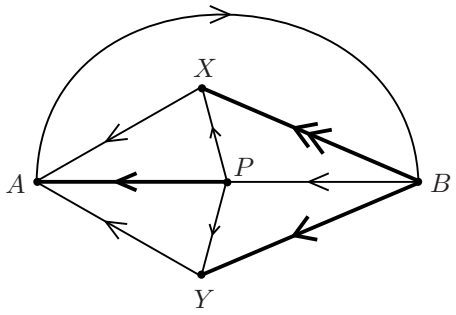

FIG. 1.1. *Schematic diagram showing the basic structure of the two heteroclinic networks studied. For clarity, the equilibrium Q is not shown, but this equilibrium has a similar role to equilibrium P except that there is a heteroclinic connection from Q to $-X$ instead of Q to X, where $-X$ is a symmetric copy of X. The remaining (conjugate) parts of the network are obtained under the action of the symmetry groups described in Section 2. Thin curves represent single (one-dimensional) heteroclinic connections and bold curves represent a two-dimensional family of connections between the relevant equilibria. The double arrowhead on the connection from B to X indicates that expansion near B in the direction of this connection is stronger than expansion in the direction of the connection from B to Y.*

In Case I, we further assume that the system is equivariant with respect to the symmetries

$$\kappa_x : (x_1, x_2, x_3, y_3) \to (x_1, x_2, -x_3, y_3), \tag{2.3}$$

$$\kappa_y : (x_1, x_2, x_3, y_3) \to (x_1, x_2, x_3, -y_3). \tag{2.4}$$

while in Case II we assume that the system is also equivariant with respect to the symmetry

$$\kappa_3 : (x_1, x_2, x_3, y_3) \to (x_1, x_2, -x_3, -y_3). \tag{2.5}$$

Note that the symmetries κ_1, κ_2, κ_x and κ_y are those used in the network in [17] while the symmetries κ_1, κ_2 and κ_3 are those used in the network in [18]; imposing the assumptions listed below ensures that Case I is precisely the network from [17] and Case II is the network from [18].

The equivariance properties of the networks cause the existence of dynamically invariant subspaces in which robust saddle–sink heteroclinic connections can occur. We make the following further assumptions about the dynamics in these subspaces, as illustrated in figure 2.1.

- **A1**: *There exist symmetry-related pairs of equilibria $\pm A$ and $\pm B$ on the x_1 and x_2 coordinate axes, respectively. Within the invariant plane $x_3 = y_3 = 0$, A is a saddle and B is a sink and there is a heteroclinic connection from A to B. See figure 2.1(a).*
- **A2:** *There exist symmetry-related pairs of equilibria $\pm X$, $\pm Y$, $\pm P$ and $\pm Q$ in the invariant plane $x_1 = x_2 = 0$. Within this subspace, $\pm X$ and $\pm Y$ are sinks, while $\pm P$ and $\pm Q$ are saddles. The eight equilibria together with the*

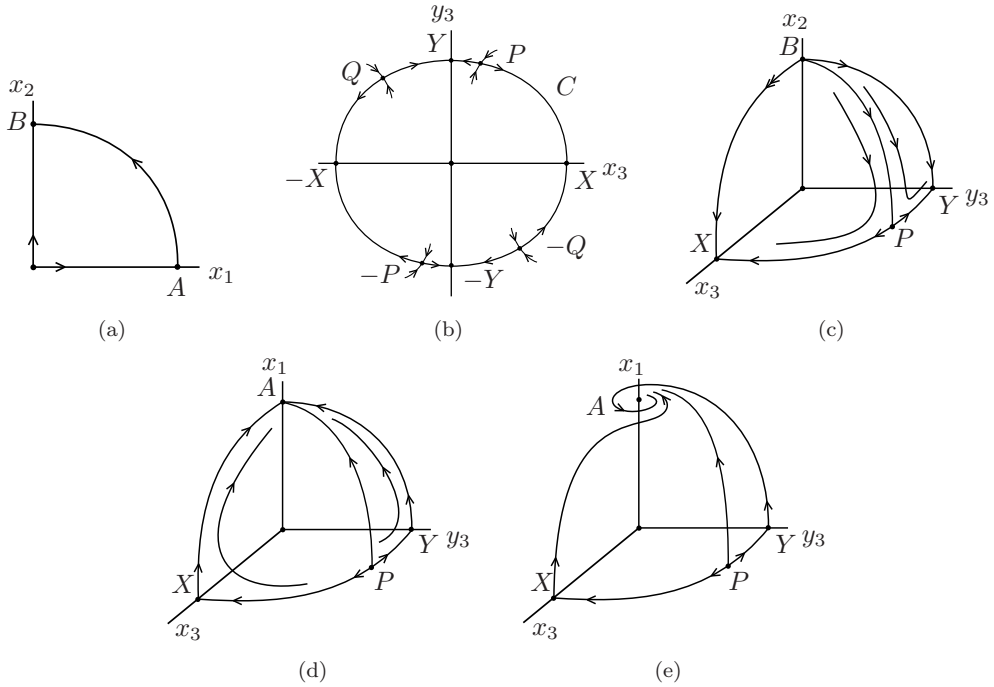

FIG. 2.1. *Dynamics within invariant subspaces of the two networks being considered. For clarity, only part of the relevant subspaces are shown in panels (a), (c), (d) and (e), with the dynamics in the omitted parts being obtained by applying the symmetries. (a) The invariant plane $x_3 = y_3 = 0$, showing the heteroclinic connection from A to B. (b) The invariant plane $x_1 = x_2 = 0$, showing the invariant circle C and the equilibria $\pm X$, $\pm Y$, $\pm P$ and $\pm Q$ that lie on C. (c) The subspace $x_1 = 0$ showing part of the two-dimensional unstable manifold of B and part of the circle C in the (x_3, y_3) plane. The equilibria $\pm X$ and $\pm Y$ are shown to lie on the coordinate axes, with the eigenvectors of the corresponding linearised flow at B aligned with the axes. In the Case I network, this situation is forced by the symmetries κ_x and κ_y. In Case II, $\pm X$ and $\pm Y$ are chosen, for convenience, to lie on the axes, but no assumption is made about the alignment of the eigenvectors. (d) The subspace $x_2 = 0$ for Case I, showing connections from X, Y and P to A. The unstable manifold of Q (not shown) behaves similarly to the unstable manifold of P. The connection from X to A (resp. Y to A) lies in the invariant plane $x_2 = y_3 = 0$ (resp. $x_2 = x_3 = 0$). (e) The subspace $x_2 = 0$ for Case II, showing spiralling of the unstable manifolds of X, Y and P into A. The unstable manifold of Q (not shown) behaves similarly. In each subspace, the flow is strongly contracting in the radial direction.*

heteroclinic connections between them make up an invariant curve C, which is topologically a circle. We hereafter refer to C as a circle, and we assume that C can be parametrised by the angle θ_3, the polar angle in the (x_3, y_3)-plane. Note that the intersections of the stable manifolds of $\pm P$ and $\pm Q$ with the invariant plane form the boundaries between the basins of attraction of $\pm X$ and $\pm Y$ in the invariant plane. Only a small part of each intersection is shown in figure 2.1(b), to avoid giving a misleading impression about the dynamics near the origin of the (x_3, y_3)-plane, but each intersection curve in fact extends to the origin of the subspace. In Case I, the x_3 and y_3 axes are

invariant and coincide with orbits of the system, but this is not necessarily so in Case II.

- **A3:** *Within the invariant subspace $x_1 = 0$, there exist two-dimensional manifolds of saddle–sink connections from B to $\pm X$ and $\pm Y$ (figure 2.1(c)). There are also one-dimensional (saddle–saddle or saddle–sink) heteroclinic connections from B to $\pm P$ and $\pm Q$ and from $\pm P$ and $\pm Q$ to $\pm X$ and $\pm Y$, as shown in figure 2.1(c). The unstable manifold of B is two-dimensional, and the stable manifolds of $\pm X$ and $\pm Y$ are each three-dimensional within the subspace.* In Case I, there is a connection from B to X (resp. from B to Y) in the subspace $x_1 = y_3 = 0$ (resp. the subspace $x_1 = x_3 = 0$).
- **A4:** *Within the invariant subspace $x_2 = 0$, there exists a two-dimensional manifold of saddle–sink connections from C to A. Within this manifold, A is either a stable node (Case I) or a stable focus (Case II). A similar manifold connects the equilibria on C to $-A$. Apart from the heteroclinic connections from $\pm P$ and $\pm Q$ to $\pm X$ and $\pm Y$, the unstable manifolds of $\pm P$ and $\pm Q$ are contained in the stable manifolds of A and $-A$. There are no equilibria other than the origin and those mentioned above lying in the subspace $x_2 = 0$. See figure 2.1(d) and (e).*
- **A5:** *Equilibrium B has real eigenvalues corresponding to dynamics in its unstable manifold, and these eigenvalues are unequal.* We do not consider the case where B has complex eigenvalues.

Assumptions **A1**–**A5** ensure the existence of the two heteroclinic networks considered in this article. The symmetries κ_1 and κ_2 ensure that x_1 and x_2 cannot change sign along a trajectory, so we consider $x_1 \geq 0$ and $x_2 \geq 0$ only. Similarly, in Case I, the symmetries κ_x and κ_y ensure that x_3 and y_3 cannot change sign along a trajectory, so in this case we can consider $x_3 \geq 0$ and $y_3 \geq 0$ only.

To simplify our analysis, we make several further assumptions. The first part of **A7** and assumptions **A8** and **A9** are automatically satisfied for Case I, but we extend them to Case II as well. **A6** is a genericity assumption and **A8** is not restrictive. Either **A7** or **A9** can always be satisfied; we restrict the dynamics by assuming both are true. **A10** is a restrictive assumption.

- **A6:** *At each equilibrium, no two of the eigenvalues of the linearisation are equal.*
- **A7:** *The two expanding eigenvectors at B lie in the x_3 and y_3 directions. Without loss of generality we assume that the eigenvalue with eigenvector pointing in the x_3 direction is larger than that corresponding to the y_3 direction.*
- **A8:** *The linearisation around A is in Jordan form.*
- **A9:** *The equilibria $\pm X$ and $\pm Y$ are, respectively, on the x_3 and y_3 coordinate axes.*
- **A10:** *At A (resp. B) the strong stable direction lies along the coordinate axis*

x_1 (resp. x_2). At each of $\pm X$, $\pm Y$, $\pm P$ and $\pm Q$, the strong stable direction lies in the (x_3, y_3) plane and is transverse to C (which is an invariant circle, by **A2***).*

We can therefore summarise the different networks we study as follows.

- In both cases, the overall network is $A \to B \to C \to A$, where, within C, trajectories can visit any of $\pm X$, $\pm Y$, $\pm P$ and $\pm Q$, although only in certain orders as indicated in figures 1.1 and 2.1. All cycles in the network contain either three or four equilibria.
- Case I is equivariant under the symmetries κ_1, κ_2, κ_x and κ_y, and the linearisation of the vector field at each equilibrium has only real eigenvalues.
- Case II is equivariant under the symmetries κ_1, κ_2 and κ_3, and the linearisation at equilibrium A has a pair of complex conjugate eigenvalues with negative real part.

3. Maps for the dynamics near the heteroclinic networks. We follow the standard procedure for modelling the dynamics near a heteroclinic network, i.e., we construct return maps defined on various cross-sections in $\mathbb{R}^4$ and analyze the dynamics of these maps. Cross-sections transverse to the connection from A to B are of special interest, since all trajectories lying near one of our networks must pass through such a cross-section and so maps defined on such a cross-section contain information about the asymptotic stability of the network as a whole. However, in our investigation of resonance bifurcations, it will be important to consider situations in which the network has more subtle stability properties, in which case we will be interested in return maps defined on cross-sections transverse to other heteroclinic connections.

In Section 3.1 we give details of the coordinates, cross-sections, and local maps (valid near equilibria) we use in construction of the return maps. Apart from the local map near A in Case I, these are the same as the maps found in [18]. In Section 3.2 we derive global maps (valid near heteroclinic connections between equilibria); these are the same as the global maps found in [18] apart from some additional constraints needed for Case I. The local and global maps we define are consistent with those used in [17], but have a more general form (and use different notation), since here the maps are designed to capture the behaviour near the whole heteroclinic network, whereas in [17] the analysis focussed on two distinguished cycles (called the ξ_3-cycle and the ξ_4-cycle in [17], corresponding to the heteroclinic cycles through X and Y in the notation of this article).

In principle, the local and global maps can be composed in an appropriate order to obtain return maps modelling the dynamics near our networks. However, because we wish our maps to keep track of a continuum of heteroclinic cycles in network, it turns out that we are unable to derive explicit forms for some of the local maps and hence for the return map as a whole. However, we are able to obtain approximations of the maps for particular ranges of the coordinates in our maps, and this is sufficient

for us to be able to extract results about resonance.

3.1. Coordinates, cross-sections, and local maps. Near A and B, we define local coordinates that place the equilibrium at the origin. We write x_i or y_i if the local coordinate is the same as the corresponding global coordinate, and use u_i for the local coordinate otherwise. We use polar coordinates when it is more convenient: (x_3, y_3) becomes (r_3, θ_3), where $x_3 = r_3 \cos\theta_3$ and $y_3 = r_3 \sin\theta_3$, and u_3 measures the distance within the x_3-y_3 subspace from the invariant circle C. Assumptions **A7** and **A8** guarantee that the coordinate axes are aligned with the eigenvectors of the relevant linearised system.

Near A, the linearised flow in Case I is given by:

$$\dot{u}_1 = -r_A u_1,\ \dot{x}_2 = e_A x_2,\ \dot{x}_3 = -c_{Ax} x_3,\ \dot{y}_3 = -c_{Ay} y_3, \tag{3.1}$$

where r_A, e_A, c_{Ax} and c_{Ay} are positive constants. The letters e, c and r in these constants refer to the expanding, contracting and radial directions, as defined by [21]. In Case II, the linearised flow near A is given by:

$$\dot{u}_1 = -r_A u_1,\ \dot{x}_2 = e_A x_2,\ \dot{x}_3 = -c_A x_3 - \omega y_3,\ \dot{y}_3 = \omega x_3 - c_A y_3, \tag{3.2}$$

where r_A, e_A, c_A and ω are positive constants. In polar coordinates, the $\dot{x}_3$ and $\dot{y}_3$ equations give $\dot{r}_3 = -c_A r_3$ and $\dot{\theta}_3 = \omega$.

Cross-sections near A are defined as:

$$\begin{array}{rcl} \mathbf{H}_A^{\text{in}} & \equiv & \{(u_1, x_2, r_3, \theta_3) \,|\, |u_1| < h, 0 \le x_2 < h, r_3 = h, 0 \le \theta_3 < 2\pi\}, \\ \mathbf{H}_A^{\text{out}} & \equiv & \{(u_1, x_2, r_3, \theta_3) \,|\, |u_1| < h, x_2 = h, 0 \le r_3 < h, 0 \le \theta_3 < 2\pi\}. \end{array} \tag{3.3}$$

Here $0 < h \ll 1$ is a parameter small enough that the cross-sections lie within the region of approximate linear flow near A (and similarly near B and C, as required below).

In Case I, the flow near A induces a map $\phi_{A,r} : \mathbf{H}_A^{\text{in}} \to \mathbf{H}_A^{\text{out}}$, which is obtained to lowest order by integrating equations (3.1):

$$\begin{aligned} &\phi_{A,r}(u_1, x_2, h, \theta_3) \\ &\quad = \left(u_1 \left(\frac{x_2}{h}\right)^{\frac{r_A}{e_A}},\ h,\ h\left(\cos^2\theta_3 \left(\frac{x_2}{h}\right)^{2\delta_{Ax}} + \sin^2\theta_3 \left(\frac{x_2}{h}\right)^{2\delta_{Ay}}\right)^{1/2},\right. \\ &\qquad \left. \tan^{-1}\left(\tan\theta_3 \left(\frac{x_2}{h}\right)^{\delta_{Ay}-\delta_{Ax}}\right),\right) \end{aligned} \tag{3.4}$$

where $\delta_{Ax} = \frac{c_{Ax}}{e_A}$ and $\delta_{Ay} = \frac{c_{Ay}}{e_A}$. In Case II, the corresponding local map, obtained to lowest order by integrating equations (3.2), is

$$\phi_{A,c}(u_1, x_2, h, \theta_3) = \left(u_1 \left(\frac{x_2}{h}\right)^{\frac{r_A}{e_A}}, h, h\left(\frac{x_2}{h}\right)^{\delta_A}, \theta_3 - \frac{\omega}{e_A}\log\left(\frac{x_2}{h}\right)\right), \tag{3.5}$$

where $\delta_A = \frac{c_A}{e_A}$.

Near B, the linearised flow is:

$$\dot{x}_1 = -c_B x_1,\ \dot{u}_2 = -r_B u_2,\ \dot{x}_3 = e_{Bx} x_3,\ \dot{y}_3 = e_{By} y_3, \tag{3.6}$$

where r_B, e_{Bx}, e_{By}, c_B are positive constants. From **A7**, we have $e_{Bx} > e_{By}$. Cross-sections near B are defined as:

$$\begin{array}{rcl} \mathbf{H}_B^{\text{in}} & \equiv & \{(x_1, u_2, r_3, \theta_3) \,|\, x_1 = h, |u_2| < h, 0 \le r_3 < h, 0 \le \theta_3 < 2\pi\}, \\ \mathbf{H}_B^{\text{out}} & \equiv & \{(x_1, u_2, r_3, \theta_3) \,|\, 0 \le x_1 < h, |u_2| < h, r_3 = h, 0 \le \theta_3 < 2\pi\}, \end{array} \tag{3.7}$$

and the flow induces a map $\phi_B : \mathbf{H}_B^{\text{in}} \to \mathbf{H}_B^{\text{out}}$, which is obtained to lowest order by integrating equations (3.6). The map cannot be written down explicitly, but is computed as follows. First, the $\dot{x}_3$ and $\dot{y}_3$ equations are solved:

$$x_3(t) = r_3(0)\cos\theta_3(0)\, e^{e_{Bx}t}, \qquad y_3(t) = r_3(0)\sin\theta_3(0)\, e^{e_{By}t},$$

where $r_3(0)$ and $\theta_3(0)$ are the initial values of the radial coordinates (i.e., on $\mathbf{H}_B^{\text{in}}$). The trajectory crosses $\mathbf{H}_B^{\text{out}}$ when $r_3(t) = h$, so the transit time T_B is found by solving the equation

$$\left(\frac{h}{r_3(0)}\right)^2 = \cos^2\theta_3(0)\, e^{2e_{Bx}T_B} + \sin^2\theta_3(0)\, e^{2e_{By}T_B} \tag{3.8}$$

for T_B in terms of $r_3(0)$ and $\theta_3(0)$. This yields the local map $\phi_B : \mathbf{H}_B^{\text{in}} \to \mathbf{H}_B^{\text{out}}$:

$$\phi_B(h, u_2, r_3, \theta_3) = \left(he^{-c_B T_B}, u_2 e^{-r_B T_B}, h, \tan^{-1}\left(\tan\theta_3 e^{(e_{By}-e_{Bx})T_B}\right)\right). \tag{3.9}$$

For later convenience, we define $\delta_{Bx} = \frac{c_B}{e_{Bx}}$ and $\delta_{By} = \frac{c_B}{e_{By}}$.

Near the circle C we would like a local map that captures the dynamics of all orbits that pass near C. Linearization of the flow near the equilibria on C alone will be insufficient for our purposes. Instead, we use the technique described in [18] and summarised below to construct a map. Specifically, we assumed in **A2** that C can be parameterised by the angle θ_3. The rate of relaxation onto C is controlled by the θ_3-dependent quantity $-r_C(\theta_3)$. The assumption of strong contraction in the radial (r_3) direction (**A10**) means that the dynamics on C of θ_3 can be captured by an equation of the form $\dot{\theta}_3 = g(\theta_3)$, where g is a nonlinear function with $g(0) = g(\frac{\pi}{2}) = g(\pi) = g(\frac{3\pi}{2}) = 0$ (this last statement follows from assumption **A9** which stipulates that $\pm X$ and $\pm Y$ lie on the coordinate axes). There will be further zeroes of g at the values of θ_3 corresponding to $\pm P$ and $\pm Q$. These considerations mean we can model the flow near C by:

$$\dot{x}_1 = e_C(\theta_3)x_1,\ \dot{x}_2 = -c_C(\theta_3)x_2,\ \dot{u}_3 = -r_C(\theta_3)u_3,\ \dot{\theta}_3 = g(\theta_3), \tag{3.10}$$

where r_C, e_C and c_C are positive functions of θ_3.

Cross-sections near C are defined as:

$$\begin{array}{rcl} \mathbf{H}_C^{\text{in}} & \equiv & \{(x_1, x_2, u_3, \theta_3) \,|\, 0 \le x_1 < h, x_2 = h, |u_3| < h, 0 \le \theta_3 < 2\pi\}, \\ \mathbf{H}_C^{\text{out}} & \equiv & \{(x_1, x_2, u_3, \theta_3) \,|\, x_1 = h, 0 \le x_2 < h, |u_3| < h, 0 \le \theta_3 < 2\pi\}. \end{array} \tag{3.11}$$

The local flow near C induces a map $\phi_C : \mathbf{H}_C^{\text{in}} \to \mathbf{H}_C^{\text{out}}$. We cannot write down the map explicitly, but it is computed as follows. First, the $\dot{\theta}_3$ equation is solved using an initial condition $\theta_3(0)$, yielding $\theta_3(t)$. Then the $\dot{x}_1$ and $\dot{x}_2$ equations are solved:

$$x_1(t) = x_1(0) \exp\left(\int_0^t e_C(\theta_3(t'))\, dt'\right), \qquad x_2(t) = h \exp\left(-\int_0^t c_C(\theta_3(t'))\, dt'\right).$$

The trajectory crosses $\mathbf{H}_C^{\text{out}}$ when $x_1(t) = h$, so the transit time T_C can be found by solving

$$\int_0^{T_C} e_C(\theta_3(t'))\, dt' = -\log\left(\frac{x_1(0)}{h}\right) \tag{3.12}$$

for T_C in terms of the initial values $x_1(0)$ and $\theta_3(0)$ on $\mathbf{H}_C^{\text{in}}$. Then the local map $\phi_C : \mathbf{H}_C^{\text{in}} \to \mathbf{H}_C^{\text{out}}$ is given by

$$\phi_C(x_1, h, u_3, \theta_3) = \left(h, h \exp\left(-\int_0^{T_C} c_C(\theta_3(t'))\, dt'\right), u_3(T_C), \theta_3(T_C)\right), \tag{3.13}$$

where $u_3(T_C) = u_3 \exp\left(-\int_0^{T_C} r_C(\theta_3(t'))\, dt'\right)$. For later convenience, we define δ_{CX} and δ_{CY} to be the ratio $\frac{c_C(\theta_3)}{e_C(\theta_3)}$ evaluated at the points X and Y respectively.

As noted above, neither of the maps ϕ_B and ϕ_C can be written down explicitly. In the case of ϕ_B, this is because we cannot write down an explicit solution of (3.8) for the transit time T_B. In the case of ϕ_C, the nonlinear evolution of θ_3 on C is not known explicitly. In section 4.1 we make assumptions about the flow near C and are then able to make approximations to the local maps in order to compute stability and bifurcation properties of the network.

3.2. Global maps. To construct global maps Ψ_{ij} that approximate the dynamics near heteroclinic connections of the networks, we linearise the dynamics about the unstable manifold leaving each of A, B and C. In doing so, we allow for the fact that the unstable manifold of A is one-dimensional, but the unstable manifolds of B and C are two-dimensional. The different equivariance properties of the vector fields for our different networks result in different constraints on the global maps for Case I and II.

The heteroclinic connection from A to B intersects $\mathbf{H}_A^{\text{out}}$ at $(u_1, x_2, x_3, y_3) = (0, h, 0, 0)$, and intersects $\mathbf{H}_B^{\text{in}}$ at $(x_1, u_2, x_3, y_3) = (h, \epsilon_B, 0, 0)$, for a small constant ϵ_B. Without loss of generality, we assume that $\epsilon_B \neq 0$. Here and below, the ϵ parameters give the value of the local radial coordinate at the intersection of the heteroclinic connection with the incoming section. These turn out to play no role at leading order, which is consistent with results about radial eigenvalues for heteroclinic cycles [21].

Generically, the dynamics near the heteroclinic connection will be (to lowest order, and in cartesian coordinates) an affine linear transformation. In polar coordinates, this yields, at leading order:

$$\Psi_{AB}(u_1, h, r_3, \theta_3) = (h, \epsilon_B, D_B(\theta_3) r_3, \bar{\theta}_B(\theta_3)), \tag{3.14}$$

where $D_B(\theta_3)$ is an order-one function of θ_3 and $\bar{\theta}_B(\theta_3)$ is an order-one function of θ_3. Invariance of the map under the symmetry κ_3 (for Case II) has the same effect on the form of the map as invariance under κ_x and κ_y (Case I), i.e., it ensures that there is no constant term or linear dependence on u_1 in the r_3-component. Thus, the form of Ψ_{AB} given above is valid for both the heteroclinic networks we consider. However, in Case I, the invariance of the x_3 and y_3 coordinate planes requires some additional constraints on the function $\bar{\theta}_B(\theta_3)$. Specifically, in Case I, $\bar{\theta}_B(0) = 0$, $\bar{\theta}_B(\frac{\pi}{2}) = \frac{\pi}{2}$, $\bar{\theta}_B(\pi) = \pi$ and $\bar{\theta}_B(\frac{3\pi}{2}) = \frac{3\pi}{2}$. In both cases, the overall effect of the map Ψ_{AB} is to multiply the small variable r_3 by an order-one function of θ_3, and to map the outgoing angle θ_3 to an incoming angle $\bar{\theta}_B(\theta_3)$.

The two-dimensional unstable manifold of B intersects $\mathbf{H}_B^{\text{out}}$ at $(x_1, u_2, r_3, \theta_3) = (0, 0, h, \theta_3)$ for $0 \leq \theta_3 < 2\pi$, and intersects $\mathbf{H}_C^{\text{in}}$ at $(x_1, x_2, u_3, \theta_3) = (0, h, \epsilon_C(\theta_3), \bar{\theta}_C(\theta_3))$, where ϵ_C is a small function of θ_3 and $\bar{\theta}_C$ is an order-one function of θ_3. To leading order in x_1 and u_2, we find:

$$\Psi_{BC}(x_1, u_2, h, \theta_3) = \left(D_C(\theta_3)x_1, h, \epsilon_C(\theta_3), \bar{\theta}_C(\theta_3)\right), \tag{3.15}$$

where $D_C(\theta_3)$ is an order-one function of θ_3. As for the map Ψ_{AB}, in Case I there are additional constraints on the function $\bar{\theta}_C$ due to the invariance of the coordinate axes. Specifically, in Case I, $\bar{\theta}_C(0) = 0$, $\bar{\theta}_C(\frac{\pi}{2}) = \frac{\pi}{2}$, $\bar{\theta}_C(\pi) = \pi$ and $\bar{\theta}_C(\frac{3\pi}{2}) = \frac{3\pi}{2}$. In both cases, we assume without loss of generality that $\epsilon_C(\theta_3) \neq 0$ for any θ_3. The function $\epsilon_C(\theta_3)$ plays a similar role to the constant ϵ_B in (3.14), except that it takes on a different value for each heteroclinic connection and so is a function of θ_3. In both cases, the overall effect of (3.15) is to multiply the small variable x_1 by an order-one function of θ_3, and to map the outgoing angle θ_3 to an incoming angle $\bar{\theta}_C(\theta_3)$.

The unstable manifold of C is two-dimensional; it intersects $\mathbf{H}_C^{\text{out}}$ along the curve $(x_1, x_2, u_3, \theta_3) = (h, 0, 0, \theta_3)$, where $0 \leq \theta_3 < 2\pi$, and it intersects $\mathbf{H}_A^{\text{in}}$ at $(u_1, x_2, r_3, \theta_3) = (\epsilon_A(\theta_3), 0, h, \bar{\theta}_A(\theta_3))$, where ϵ_A is a small function of θ_3 and $\bar{\theta}_A$ is an order-one function of θ_3. For small x_2 and u_3, we have:

$$\Psi_{CA}(h, x_2, u_3, \theta_3) = \left(\epsilon_A(\theta_3), D_A(\theta_3)x_2, h, \bar{\theta}_A(\theta_3)\right), \tag{3.16}$$

where $D_A(\theta_3)$ is an order-one function of θ_3. In Case I, invariance of the coordinate axes means that $\bar{\theta}_A(0) = 0$, $\bar{\theta}_A(\frac{\pi}{2}) = \frac{\pi}{2}$, $\bar{\theta}_A(\pi) = \pi$ and $\bar{\theta}_A(\frac{3\pi}{2}) = \frac{3\pi}{2}$. In both cases, the overall effect of Ψ_{CA} is to multiply the small variable x_2 by an order-one function of θ_3, and to map the outgoing angle θ_3 to an incoming angle $\bar{\theta}_A$.

4. Preliminary analysis of maps. In order to make further progress, it is necessary to introduce some approximations and simplifications to the local maps.

In section 4.1, we construct approximations to the local maps near A and B valid close to the X and Y directions. We also assume a simple form for the dynamics near C; we believe that this simplification will not qualitatively change our results. Throughout this section, we set $h = 1$ without loss of generality; this is equivalent to rescaling the local coordinates introduced in the previous section.

Once the approximations are made, we are then (in sections 4.2 and 4.4) able to compose the maps and compute a quantity we call $\delta(\theta_3)$ which gives the rate of contraction or expansion of trajectories near the network, as a function of the coordinate θ_3. This quantity plays a similar role to the ratio of contracting to expanding eigenvalues used to determine stability of some heteroclinic cycles. However, because we are working with a network, the ratio is dependent on the particular route taken around the network. As part of these calculations, we find it useful to define:

$$\delta_X = \delta_{Ax}\delta_{Bx}\delta_{CX}, \qquad \delta_Y = \delta_{Ay}\delta_{By}\delta_{CY}$$

where in Case II, $\delta_{Ax} = \delta_{Ay} = \delta_A$.

4.1. Approximate local maps. First we look at the map for the dynamics near A in Case I, $\phi_A : (u_1, x_2, 1, \theta_3) \to (u_1, 1, r_3, \theta_3)$. In the following, the notation $\theta^{A_{\text{in}}}$ (resp. $\theta^{A_{\text{out}}}$) refers to the value of θ_3 on $\mathbf{H}_A^{\text{in}}$ (resp. $\mathbf{H}_A^{\text{out}}$), while x_2 (resp. r_3) represents the value of the second (resp. third) coordinate on $\mathbf{H}_A^{\text{in}}$ (resp. $\mathbf{H}_A^{\text{out}}$). Then, from (3.4), we have

$$r_3 = \left(\cos^2\theta^{A_{\text{in}}}\, x_2^{2\delta_{Ax}} + \sin^2\theta^{A_{\text{in}}}\, x_2^{2\delta_{Ay}}\right)^{1/2} \tag{4.1}$$

and

$$\tan\theta^{A_{\text{out}}} = \tan\theta^{A_{\text{in}}}\, x_2^{\delta_{Ay}-\delta_{Ax}}, \tag{4.2}$$

where r_3 and x_2 are both small. When $\theta^{A_{\text{in}}} = 0$ (resp. $\frac{\pi}{2}$), we have $\log r_3 = \delta_{Ax}\log x_2$ (resp. $\log r_3 = \delta_{Ay}\log x_2$).

Expression (4.1) can be rewritten as

$$r_3 = \left|\cos\theta^{A_{\text{in}}}\right|\, x_2^{\delta_{Ax}}\left(1 + \tan^2\theta^{A_{\text{in}}}\, x_2^{2(\delta_{Ay}-\delta_{Ax})}\right)^{1/2}$$

so we have

$$\frac{\log r_3}{\log x_2} = \delta_{Ax} + \frac{\log\left|\cos\theta^{A_{\text{in}}}\right|}{\log x_2} + \frac{1}{2}\frac{\log\left(1 + \tan^2\theta^{A_{\text{in}}}\, x_2^{2(\delta_{Ay}-\delta_{Ax})}\right)}{\log x_2}.$$

Note that the term inside the logarithm may be large or small. We further approximate this later as appropriate.

In the case of complex eigenvalues at A, the local map (3.5) gives:

$$\frac{\log r_3}{\log x_2} = \delta_A, \qquad \theta^{A_{\text{out}}} = \theta^{A_{\text{in}}} - \frac{\omega}{e_A}\log x_2. \tag{4.3}$$

Approximating the local map at B is complicated by the need to solve (3.8) for the transit time T_B. At B, we have by assumption **A7** that $e_{Bx} > e_{By}$, and so $\delta_{Bx} < \delta_{By}$. Let $\theta^{B_{\text{in}}}$ (resp. $\theta^{B_{\text{out}}}$) be the value of θ_3 on $\mathbf{H}_B^{\text{in}}$ (resp. $\mathbf{H}_B^{\text{out}}$) and denote

by r_3 (resp. x_1) the value of the third (resp. first) coordinate on $\mathbf{H}_B^{\text{in}}$ (resp. $\mathbf{H}_B^{\text{out}}$). We can then rewrite (3.8) as:

$$r_3^{-2} = \cos^2\theta^{B_{\text{in}}}\, e^{2e_{Bx}T_B}\left(1+\tan^2\theta^{B_{\text{in}}}\, e^{2(e_{By}-e_{Bx})T_B}\right),$$

where r_3 is small.

As long as $\theta^{B_{\text{in}}}$ is not too close to $\frac{\pi}{2}$ or $\frac{3\pi}{2}$, the second term in the brackets is small compared to the first; we drop this term and solve for T_B, finding $T_B = -\frac{1}{e_{Bx}}\log r_3|\cos\theta^{B_{\text{in}}}|$. The term that was dropped is small (with this value of T_B) so long as $|\cot\theta^{B_{\text{in}}}| \gg \theta^{\epsilon_B}$, where

$$\theta^{\epsilon_B} \equiv r_3^{\frac{\delta_{By}}{\delta_{Bx}}-1} \ll 1 \qquad (\delta_{By} > \delta_{Bx}). \tag{4.4}$$

When $|\cot\theta^{B_{\text{in}}}| \ll \theta^{\epsilon_B}$ (i.e., $\theta^{B_{\text{in}}}$ is close to $\frac{\pi}{2}$ or $\frac{3\pi}{2}$), we cannot drop the second term but instead approximately solve (3.8), finding

$$T_B = -\frac{1}{e_{By}}\log\left(r_3\left|\sin\theta^{B_{\text{in}}}\right|\left(1+\frac{1}{2}\cot^2\theta^{B_{\text{in}}}\left(r_3\sin\theta^{B_{\text{in}}}\right)^{2\left(1-\frac{\delta_{By}}{\delta_{Bx}}\right)}\right)\right).$$

From these expressions, we can use (3.9) to find the exit values of x_1 and θ_3 after ϕ_B:

$$\frac{\log x_1}{\log r_3} \sim \begin{cases} \delta_{Bx} + \delta_{Bx}\dfrac{\log\left|\cos\theta^{B_{\text{in}}}\right|}{\log r_3}, & \left|\cot\theta^{B_{\text{in}}}\right| \gg \theta^{\epsilon_B}, \\ \delta_{By} + \delta_{By}\dfrac{\frac{1}{2}\cot^2\theta^{B_{\text{in}}}\, r_3^{2(1-\frac{\delta_{By}}{\delta_{Bx}})}}{\log r_3}, & \left|\cot\theta^{B_{\text{in}}}\right| \ll \theta^{\epsilon_B}, \end{cases} \tag{4.5}$$

and

$$\frac{\tan\theta^{B_{\text{out}}}}{\tan\theta^{B_{\text{in}}}} \sim \begin{cases} \left(r_3\left|\cos\theta^{B_{\text{in}}}\right|\right)^{1-\frac{\delta_{Bx}}{\delta_{By}}}, & \left|\cot\theta^{B_{\text{in}}}\right| \gg \theta^{\epsilon_B}, \\ r_3^{\frac{\delta_{By}}{\delta_{Bx}}-1}\left(1+\frac{1}{2}\cot^2\theta^{B_{\text{in}}}\, r_3^{2(1-\frac{\delta_{By}}{\delta_{Bx}})}\left(\frac{\delta_{By}}{\delta_{Bx}}-1\right)\right), & \left|\cot\theta^{B_{\text{in}}}\right| \ll \theta^{\epsilon_B}, \end{cases} \tag{4.6}$$

where x_1 and r_3 are both small.

There are three obstacles to estimating the local map near C: the θ_3 dynamics is given by $\dot\theta_3 = g(\theta_3)$, where $g(\theta_3)$ is unknown, and $e_C(\theta_3)$ and $c_C(\theta_3)$ are unknown. In order to make progress, we take simple forms for $g(\theta_3)$, $e_C(\theta_3)$ and $c_C(\theta_3)$ that allow us to solve for $\theta_3(t)$ and to compute the required integrals. We believe that these simplifications will not qualitatively change our results.

In the following we let $\theta^{C_{\text{in}}}$ (resp. $\theta^{C_{\text{out}}}$) be the value of θ_3 on $\mathbf{H}_C^{\text{in}}$ (resp. $\mathbf{H}_C^{\text{out}}$) and denote by x_1 (resp. x_2) the value of the first (resp. second) coordinate on $\mathbf{H}_C^{\text{in}}$ (resp. $\mathbf{H}_C^{\text{out}}$).

We first assume that e_C does not depend on θ_3. This allows us to calculate the transit time from $\mathbf{H}_C^{\text{in}}$ to $\mathbf{H}_C^{\text{out}}$:

$$T_C = -\frac{1}{e_C}\log x_1.$$

We then assume that g takes a very simple form, i.e., we choose $g(\theta_3) = -\frac{\lambda}{4}\sin(4\theta_3)$, with $\lambda > 0$. Then X and Y are at $\theta_3 = 0$ and $\frac{\pi}{2}$, and P is at $\theta_3 = \frac{\pi}{4}$. With this form for g we can solve $\dot{\theta}_3 = g(\theta_3)$, and find

$$\tan 2\theta_3(t) = \tan 2\theta^{C_{\rm in}}\, e^{-\lambda t},$$

taking $\theta_3(0) = \theta^{C_{\rm in}}$. With $\theta_3(T_C) = \theta^{C_{\rm out}}$, we find

$$\tan 2\theta^{C_{\rm out}} = \tan 2\theta^{C_{\rm in}}\, x_1^{\frac{\lambda}{e_C}}, \tag{4.7}$$

It would be tempting to assume also that c_C does not depend on θ_3; however, this turns out to be too restrictive. Instead, we write

$$c_C(\theta_3) = \frac{c_{CX} + c_{CY}}{2} + \frac{c_{CX} - c_{CY}}{2}\cos 2\theta_3; \tag{4.8}$$

this ensures $c_C(0) = c_C(\pi) = c_{CX}$ and $c_C(\frac{\pi}{2}) = c_C(\frac{3\pi}{2}) = c_{CY}$. With this, the exit value of x_2 is $\exp\left(-\int_0^{T_C} c_C(\theta_3(t'))\,dt'\right)$. From above, we know $\tan 2\theta_3(t)$ explicitly, so $\cos(2\theta_3) = \pm(1 + \tan^2(2\theta^{C_{\rm in}})e^{-2\lambda t})^{-1/2}$, where we take the positive square root if $0 \le \theta^{C_{\rm in}} < \frac{\pi}{4}$ and the negative square root if $\frac{\pi}{4} < \theta^{C_{\rm in}} \le \frac{\pi}{2}$. Note that

$$\int \frac{1}{\sqrt{1 + K^2 e^{-2\lambda t}}} dt = -\frac{1}{2\lambda}\log\left(\frac{\sqrt{1 + K^2 e^{-2\lambda t}} - 1}{\sqrt{1 + K^2 e^{-2\lambda t}} + 1}\right)$$

and so we find

$$\frac{\log x_2}{\log x_1} = \frac{\delta_{CX} + \delta_{CY}}{2} \pm \frac{c_{CX} - c_{CY}}{4\lambda \log x_1}\log\left(\frac{\left(\sqrt{1 + \tan^2 2\theta^{C_{\rm in}}\, x_1^{\frac{2\lambda}{e_C}}} - 1\right)\left(|\sec 2\theta^{C_{\rm in}}| + 1\right)}{\left(\sqrt{1 + \tan^2 2\theta^{C_{\rm in}}\, x_1^{\frac{2\lambda}{e_C}}} + 1\right)\left(|\sec 2\theta^{C_{\rm in}}| - 1\right)}\right)$$

where x_2 and x_1 are both small. As before, the plus sign is taken if $0 \le \theta^{C_{\rm in}} < \frac{\pi}{4}$ and the minus sign is taken if $\frac{\pi}{4} < \theta^{C_{\rm in}} \le \frac{\pi}{2}$.

If we are away from $\theta^{C_{\rm in}} = \frac{\pi}{4}$, such that $\tan^2 2\theta^{C_{\rm in}}\, x_1^{\frac{2\lambda}{e_C}} \ll 1$, then we can approximate the function above as:

$$\frac{\log x_2}{\log x_1} \sim \begin{cases} \delta_{CX} - \frac{c_{CX} - c_{CY}}{2\lambda \log x_1}\log\left(1 - \tan^2\theta^{C_{\rm in}}\right), & 0 \le \theta^{C_{\rm in}} < \frac{\pi}{4}, \\ \frac{1}{2}(\delta_{CX} + \delta_{CY}), & \theta^{C_{\rm in}} = \frac{\pi}{4}, \\ \delta_{CY} + \frac{c_{CX} - c_{CY}}{2\lambda \log x_1}\log\left(1 - \cot^2\theta^{C_{\rm in}}\right), & \frac{\pi}{4} < \theta^{C_{\rm in}} \le \frac{\pi}{2}, \end{cases} \tag{4.9}$$

where x_2 and x_1 are both small, and the bounds near $\frac{\pi}{4}$ are taken to mean that $\tan 2\theta^{C_{\rm in}}\, x_1^{\frac{\lambda}{e_C}} \ll 1$.

4.2. Composing the maps: Case I. In this subsection we consider the return maps for Case I. In section 4.2.1 we compose the maps starting on each of $\mathbf{H}^{\text{in}}_A$, $\mathbf{H}^{\text{in}}_B$ and $\mathbf{H}^{\text{in}}_C$, and for each return map, we focus on the θ_3 component. We argue that in the parameter regimes of interest, the return maps give the same dynamics regardless of which section we start on. Thus in section 4.2.2, where we consider the other component of the return map, we need only consider the return map starting on $\mathbf{H}^{\text{in}}_A$. Note that away from resonance when the network as a whole is attracting, this is not the case — in order to fully describe the dynamics of trajectories near the network, the composition of the maps must be considered starting on all three Poincaré sections. This observation was made in [17] and more details can be found in that article. A second example of this behaviour was also seen in [24] for a more complicated heteroclinic network.

4.2.1. θ_3 component. As in the previous section, we denote by $\theta^{A_{\text{in}}}$ (resp. $\theta^{A_{\text{out}}}$) the value of θ_3 on $\mathbf{H}^{\text{in}}_A$ (resp. $\mathbf{H}^{\text{out}}_A$), and by $\hat{\theta}^{A_{\text{in}}}$ the value of θ_3 after one application of the return map from $\mathbf{H}^{\text{in}}_A$ to itself; $\hat{\theta}^{A_{\text{in}}}$ will typically depend on $\theta^{A_{\text{in}}}$ and x_2. The symbols $\hat{\theta}^{B_{\text{in}}}$ and $\hat{\theta}^{C_{\text{in}}}$ are defined in an analogous way on the cross-sections $\mathbf{H}^{\text{in}}_B$ and $\mathbf{H}^{\text{in}}_C$. Without introducing ambiguity, we also write x_2 for the value of x_2 on $\mathbf{H}^{\text{in}}_A$, r_3 for the value of r_3 on $\mathbf{H}^{\text{in}}_B$ and x_1 for the value of x_1 on $\mathbf{H}^{\text{in}}_C$.

We wish to compute the derivative of $\hat{\theta}^{A_{\text{in}}}$ with respect to $\theta^{A_{\text{in}}}$ at two special values of θ_3, those corresponding to the invariant subspaces containing the heteroclinic cycles through X and Y, and similarly for derivatives of $\hat{\theta}^{B_{\text{in}}}$ and $\hat{\theta}^{C_{\text{in}}}$. We can compute these derivatives without computing the entire return map, and doing so greatly simplifies the computation (which we give below) of the return map for general values of θ_3. Simple calculations following from section 4.1 give

$$\frac{d\theta^{A_{\text{out}}}}{d\theta^{A_{\text{in}}}} = \begin{cases} x_2^{\delta_{CY}-\delta_{CX}}, & \theta^{A_{\text{in}}} = 0 \\ x_2^{\delta_{CX}-\delta_{CY}}, & \theta^{A_{\text{in}}} = \frac{\pi}{2} \end{cases}$$

$$\frac{d\theta^{B_{\text{out}}}}{d\theta^{B_{\text{in}}}} = \begin{cases} r_3^{1-\frac{\delta_{Bx}}{\delta_{By}}}, & \theta^{B_{\text{in}}} = 0 \\ r_3^{1-\frac{\delta_{By}}{\delta_{Bx}}}, & \theta^{B_{\text{in}}} = \frac{\pi}{2} \end{cases}$$

and

$$\frac{d\theta^{C_{\text{out}}}}{d\theta^{C_{\text{in}}}} = x_1^{\frac{\lambda}{e_C}}, \quad \theta^{C_{\text{in}}} = 0, \frac{\pi}{2}.$$

Furthermore, at $\theta_3 = 0$,

$$r_3 = x_2^{\delta_{Ax}}, \quad x_1 = r_3^{\delta_{Bx}}, \quad x_2 = x_1^{\delta_{CX}}$$

and at $\theta_3 = \frac{\pi}{2}$

$$r_3 = x_2^{\delta_{Ay}}, \quad x_1 = r_3^{\delta_{By}}, \quad x_2 = x_1^{\delta_{CY}}.$$

We can now compute the derivatives of the θ_3 components of the full return map at 0 and $\frac{\pi}{2}$; we use the chain rule and make the assumption that the global parts of the maps only affect the derivatives by an $\mathcal{O}(1)$ amount. We find that we get different results, depending on the initial cross-section for the return map. This is consistent with the results derived in [17] using different methods. If we start on $\mathbf{H}_A^{\text{in}}$ we have

$$\frac{d\hat{\theta}^{A_{\text{in}}}}{d\theta^{A_{\text{in}}}} = \begin{cases} x_2^{\nu_{AX}}, & \theta^{A_{\text{in}}} = 0 \\ x_2^{\nu_{AY}}, & \theta^{A_{\text{in}}} = \dfrac{\pi}{2}. \end{cases}$$

Starting on $\mathbf{H}_B^{\text{in}}$ and $\mathbf{H}_C^{\text{in}}$ we have, respectively,

$$\frac{d\hat{\theta}^{B_{\text{in}}}}{d\theta^{B_{\text{in}}}} = \begin{cases} r_3^{\nu_{BX}}, & \theta^{B_{\text{in}}} = 0 \\ r_3^{\nu_{BY}}, & \theta^{B_{\text{in}}} = \dfrac{\pi}{2} \end{cases}$$

and

$$\frac{d\hat{\theta}^{C_{\text{in}}}}{d\theta^{C_{\text{in}}}} = \begin{cases} x_1^{\nu_{CX}}, & \theta^{C_{\text{in}}} = 0 \\ x_1^{\nu_{CY}}, & \theta^{C_{\text{in}}} = \dfrac{\pi}{2} \end{cases}$$

where

$$\begin{aligned}
\nu_{AX} &= \delta_{Ay} - \delta_{Ax}\frac{\delta_{Bx}}{\delta_{By}} + \frac{\lambda}{e_C}\delta_{Ax}\delta_{Bx}, \\
\nu_{AY} &= \delta_{Ax} - \delta_{Ay}\frac{\delta_{By}}{\delta_{Bx}} + \frac{\lambda}{e_C}\delta_{Ay}\delta_{By}, \\
\nu_{BX} &= -\frac{\delta_{Bx}}{\delta_{By}} + \frac{\lambda}{e_C}\delta_{Bx} + \delta_{Ay}\delta_{Bx}\delta_{CX} + (1-\delta_X), \\
\nu_{BY} &= -\frac{\delta_{By}}{\delta_{Bx}} + \frac{\lambda}{e_C}\delta_{By} + \delta_{Ax}\delta_{By}\delta_{CY} + (1-\delta_Y), \\
\nu_{CX} &= \frac{\lambda}{e_C} + \delta_{Ay}\delta_{CX} - \delta_{Ax}\delta_{CX}\frac{\delta_{Bx}}{\delta_{By}}, \\
\nu_{CY} &= \frac{\lambda}{e_C} + \delta_{Ax}\delta_{CY} - \delta_{Ay}\delta_{CY}\frac{\delta_{By}}{\delta_{Bx}}.
\end{aligned}$$

Note that the sign of the appropriate ν_{ij} determines the slope of the θ_3 part of the return map at $\theta_3 = 0$ or $\theta_3 = \frac{\pi}{2}$. This in turn determines the stability properties of the invariant subspaces at $\theta_3 = 0$ or $\theta_3 = \frac{\pi}{2}$ in the full return map.

The following relations hold between the constants defined above:

$$\begin{aligned}
\nu_{AX}\delta_{CX} &= \nu_{CX} + \frac{\lambda}{e_C}(\delta_X - 1), & \nu_{AY}\delta_{CY} &= \nu_{CY} + \frac{\lambda}{e_C}(\delta_Y - 1), \\
\nu_{BX}\delta_{Ax} &= \nu_{AX} + \left(\frac{\delta_{Ay}}{\delta_{Ax}} - 1\right)(\delta_X - 1), & \nu_{BY}\delta_{Ay} &= \nu_{AY} + \left(\frac{\delta_{Ax}}{\delta_{Ay}} - 1\right)(\delta_Y - 1), \\
\nu_{CX}\delta_{Bx} &= \nu_{BX} + \left(1 - \frac{\delta_{Bx}}{\delta_{By}}\right)(\delta_X - 1), & \nu_{CY}\delta_{By} &= \nu_{BY} + \left(1 - \frac{\delta_{By}}{\delta_{Bx}}\right)(\delta_Y - 1).
\end{aligned}$$

If δ_X is sufficiently close to 1, then ν_{AX}, ν_{BX} and ν_{CX} all have the same sign; since we are interested in resonance phenomena for which $\delta_X \approx 1$, we will assume this is

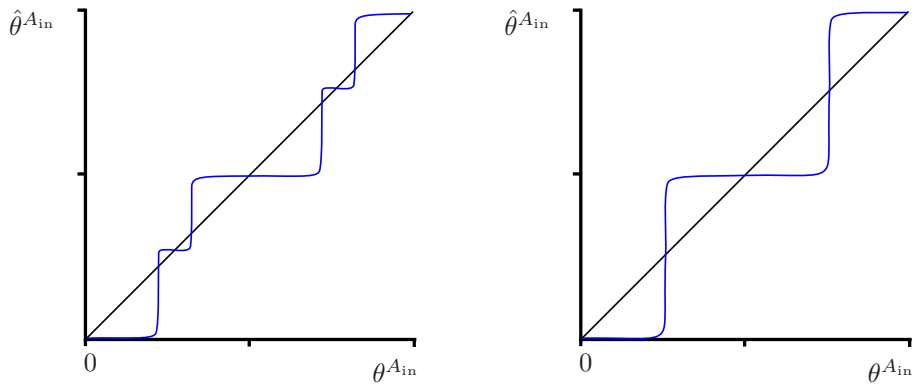

(a) $\nu_{AX}, \nu_{AY} > 0$ (b) $\nu_{AX} > 0$, $\nu_{AY} < 0$

FIG. 4.1. *Case I: θ_3 component of the full return map, starting on $\mathbf{H}^{\text{in}}_A$ with a fixed value of x_2, for two choices of signs of the ν_{ij}.*

the case. Similarly, if δ_Y is sufficiently close to 1, then ν_{AY}, ν_{BY} and ν_{CY} all have the same sign; we will assume in the following that this is the case. This assumption means that the stabilities of the invariant subspaces at $\theta_3 = 0$ and $\theta_3 = \frac{\pi}{2}$ are independent of the section on which the composition of the return map starts.

Away from resonance, it is possible that, for example, $\nu_{AX} > 0$ and $\nu_{BX} < 0$. It is precisely this type of condition which gives the very delicate stability properties of the subcycles of the network that is seen in [17]. There, a subcycle may appear to be attracting if nearby trajectories are observed as they pass through one Poincaré section, but may seem to be repelling if trajectories are observed at a different Poincaré section. This type of stability cannot be seen for objects such as periodic orbits or equilibria in flows. In this article, we only consider the case close enough to resonance when this phenomena does not occur, and hence need only consider composing the maps starting on $\mathbf{H}^{\text{in}}_A$.

Consider first the case for which $\nu_{AX}, \nu_{AY} > 0$. Then, for fixed x_2, the graph of $\hat{\theta}^{A_{\text{in}}}$ as a function of $\theta^{A_{\text{in}}}$ has flat sections near $\theta^{A_{\text{in}}} = 0$, $\frac{\pi}{2}$, π, $\frac{3\pi}{2}$, that is, $\frac{d\hat{\theta}^{A_{\text{in}}}}{d\theta^{A_{\text{in}}}} \to 0$ as $x_2 \to 0$ at these values of $\theta^{A_{\text{in}}}$. Since almost all trajectories pass close to X, $-X$, Y or $-Y$, almost all trajectories will return to $\mathbf{H}^{\text{in}}_A$ with a value of θ_3 approximately equal to 0, $\frac{\pi}{2}$, π or $\frac{3\pi}{2}$. As a consequence, the sections of the graph of $\hat{\theta}^{A_{\text{in}}}$ between the flat sections will be steep. Figure 4.1(a) shows schematically the shape of the graph of $\hat{\theta}^{A_{\text{in}}}$ as a function of $\theta^{A_{\text{in}}}$ for trajectories with a fixed value of x_2.

The width of the small flat section near $\frac{\pi}{2}$ can be computed. Points in this part of the graph correspond to orbits which pass close to Y, and the left boundary is given by the preimage of $\frac{\pi}{2} - \theta^{\epsilon_B}$ under the map $\Psi_{AB} \circ \phi_A$, where θ^{ϵ_B} was defined in (4.4). We define θ^{ϵ_A} to be such that this preimage is $\frac{\pi}{2} - \theta^{\epsilon_A}$.

We can compute θ^{ϵ_A} using the approximations of ϕ_A given in section 4.1, and assuming the global map has only an $\mathcal{O}(1)$ effect. Since $\theta^{\epsilon_B} \ll 1$, we approximate the

ϕ_A map as

$$\begin{aligned}\log r_3 &= \delta_{Ay} \log x_2,\\ \tan\theta^{B_{\text{in}}} &= \tan\theta_3\, x_2^{\delta_{Ay}-\delta_{Ax}}.\end{aligned}$$

Approximating $\tan\theta^{\epsilon_B} \sim 1/\theta^{\epsilon_B}$ (and similarly for θ^{ϵ_A}), we have

$$\begin{aligned}\theta^{\epsilon_A} &= \theta^{\epsilon_B} (x_2)^{\delta_{Ay}-\delta_{Ax}}\\ &= r_3^{\frac{\delta_{By}}{\delta_{Bx}}-1} x_2^{\delta_{Ay}-\delta_{Ax}}\\ &= x_2^{\frac{\delta_{By}}{\delta_{Bx}}\sigma}\end{aligned}$$

where we define

$$\sigma = \delta_{Ay} - \delta_{Ax}\frac{\delta_{Bx}}{\delta_{By}}.$$

The right boundary of the flat section near $\frac{\pi}{2}$ can be found by symmetry, and so the width of the flat section near $\frac{\pi}{2}$ scales like $x_2^{\frac{\delta_{By}}{\delta_{Bx}}\sigma}$.

Now we consider other cases of the signs of ν_{AX} and ν_{AY}. Note that

$$\nu_{AX} = \sigma + \frac{\lambda}{c_{Cx}}\delta_X \quad \text{and} \quad \nu_{AY} = -\frac{\delta_{By}}{\delta_{Bx}}\sigma + \frac{\lambda}{c_{Cy}}\delta_Y.$$

Thus, if $\sigma > 0$, then $\nu_{AX} > 0$, while if $\sigma < 0$, then $\nu_{AY} > 0$, and so it is not possible to have both $\nu_{AX} < 0$ and $\nu_{AY} < 0$. This leaves the cases where ν_{AX} and ν_{AY} have opposite signs. If $\sigma > 0$, then either $\nu_{AY} > 0$, as considered above, or $\nu_{AY} < 0$, meaning that there is no small step near $\theta_3 = \frac{\pi}{2}$, and the invariant subspace $\theta_3 = \frac{\pi}{2}$ is repelling; a sketch of the θ component of the return map in this latter case is shown in figure 4.1(b).

If $\sigma < 0$, there are again two cases, similar to those described above, but with the roles of $\theta = 0$ and $\theta = \frac{\pi}{2}$ reversed. We believe the dynamics for $\sigma < 0$ will be analogous to that for $\sigma > 0$ (only with this reversal) and so consider just the case $\sigma > 0$ for the remainder of this article.

It is useful here to summarise the conditions we now have on the eigenvalue ratios in Case I.

- By assumption **A7**, we have $\delta_{Bx} < \delta_{By}$. This implies that in a neighbourhood of $\delta_X = \delta_Y = 1$ we must have $\delta_{CX}\delta_{Ax} > \delta_{CY}\delta_{Ay}$.
- We additionally choose to impose $\sigma > 0$, and specifically want this to hold when $\delta_X = \delta_Y = 1$. Since

  $$\sigma > 0 \;\Rightarrow\; \delta_{Ay}\delta_{By} > \delta_{Ax}\delta_{Bx}$$

  we require $\delta_{CX} > \delta_{CY}$ so that $\sigma > 0$ in a neighbourhood of $\delta_X = \delta_Y = 1$.

- Together these conditions imply

$$\frac{\delta_{CX}}{\delta_{CY}} > \frac{\delta_{Ay}}{\delta_{Ax}} > \frac{\delta_{Bx}}{\delta_{By}}$$

Note that $\frac{\delta_{Ay}}{\delta_{Ax}}$ could be greater or less than 1.

Fixing δ_{Bx} and imposing the requirements $\frac{\delta_{Bx}}{\delta_{By}} < 1$, $\frac{\delta_{CX}}{\delta_{CY}} > 1$ and $\sigma > 0$ still gives us the freedom to vary both δ_X and δ_Y above and below 1.

4.2.2. x_2 component. We now compose the three local and global maps starting on $\mathbf{H}_A^{\text{in}}$, using initial values of $\theta^{A_{\text{in}}}$ and x_2 with $0 \leq \theta_3 \leq \frac{\pi}{2}$ and x_2 small, and focus on what happens to the x_2 component of the map. We will eventually end up with an approximate map of the form

$$x_2 \to D x_2^{\delta}$$

where D and δ are functions depending on $\theta^{A_{\text{in}}}$ and x_2. In other words, the amount of contraction or expansion of the x_2 coordinate of an orbit in one circuit of the network will depend on the initial condition for that orbit; this is a consequence of the network structure and is different to the case for maps modelling the dynamics near a single heteroclinic cycle. To capture this effect, in the following we write down the contraction or expansion rate of each the local maps as a function of the incoming coordinates for that local map, then rewrite the incoming coordinates as a function of the initial conditions of the orbit on $\mathbf{H}_A^{\text{in}}$. Thus, the functions we obtain for the contraction rates at B and C will depend on $\theta^{A_{\text{in}}}$ and the value of x_2 on $\mathbf{H}_A^{\text{in}}$.

We use the approximate forms of the local maps derived in section 4.1, making use of the assumed form of the dynamics at C. We will also assume that the global maps multiply the small variable by a θ_3-dependent order-one constant (as described in section 3.2), so $r_3 = D_B(\theta_3) r_3^{A_{\text{out}}}$ etc., and that the θ_3 parts of the global maps do nothing, that is, $\bar{\theta}_B(\theta_3) = \theta_3$, and so $\theta^{B_{\text{in}}} = \theta^{A_{\text{out}}}$ etc.). This will give a distorted view of the correct picture, but the distortion will only be slight, since the dynamics is dominated by the local maps.

We focus our discussion on the interval $0 \leq \theta^{A_{\text{in}}} \leq \frac{\pi}{2}$; this can be extended to 2π by symmetry. To allow for this, we will include absolute values in expressions such as (for example) $\log|\cos\theta^{A_{\text{in}}}|$.

We divide the interval $0 \leq \theta^{A_{\text{in}}} \leq \frac{\pi}{2}$ into two regions, which are the different regions of validity of the approximate local maps ϕ_B and ϕ_C. The boundaries of the regions depend on the value of r_3 on $\mathbf{H}_B^{\text{in}}$ as given in (4.5). We have $\theta^{\epsilon_B} = r_3^{\frac{\delta_{By}}{\delta_{Bx}}-1}$ and the two regions are given by $\cot\theta^{B_{\text{in}}} \gg \theta^{\epsilon_B}$ and $\cot\theta^{B_{\text{in}}} \ll \theta^{\epsilon_B}$. As computed in the previous section, the two regions can also be defined on $\mathbf{H}_A^{\text{in}}$ as $\cot\theta^{A_{\text{in}}} \gg \theta^{\epsilon_A}$ and $\cot\theta^{A_{\text{in}}} \ll \theta^{\epsilon_A}$, where $\theta^{\epsilon_A} = x_2^{\frac{\delta_{By}}{\delta_{Bx}}\sigma}$.

Region 1. First, consider the region $0 \le \theta^{A_{\text{in}}} \ll \frac{\pi}{2} - \theta^{\epsilon_A}$, so $\tan\theta^{A_{\text{in}}}\, x_2^{\frac{\delta_{By}}{\delta_{Bx}}\sigma} \ll 1$. After ϕ_A and Ψ_{AB} we have

$$\begin{aligned}\tan\theta^{B_{\text{in}}} &= \tan\theta^{A_{\text{in}}}\, x_2^{\delta_{Ay}-\delta_{Ax}},\\ \log r_3 &= \log D_B + \delta_A(\theta^{A_{\text{in}}})\log x_2,\end{aligned}$$

where

$$\delta_A(\theta^{A_{\text{in}}}) = \delta_{Ax} + \frac{\log\left|\cos\theta^{A_{\text{in}}}\right|}{\log x_2} + \frac{1}{2}\frac{\log\left(1+\tan^2\theta^{A_{\text{in}}}\, x_2^{2(\delta_{Ay}-\delta_{Ax})}\right)}{\log x_2}.$$

Although $\delta_A(\theta^{A_{\text{in}}})$ depends also on $\log x_2$, we omit specifying this dependence in the argument (and in $\delta_B(\theta^{A_{\text{in}}})$ and $\delta_C(\theta^{A_{\text{in}}})$ below) to simplify the writing.

Since we are in region 1, trajectories visit the X part of the second local map. Therefore, after ϕ_B and Ψ_{BC}, we have:

$$\begin{aligned}\tan\theta^{C_{\text{in}}} &= \tan\theta^{B_{\text{in}}}\left|r_3\cos\theta^{B_{\text{in}}}\right|^{1-\frac{\delta_{Bx}}{\delta_{By}}}\\ \log x_1 &= \log D_C + \delta_B(\theta^{A_{\text{in}}})\log r_3\end{aligned}$$

where

$$\begin{aligned}\delta_B(\theta^{A_{\text{in}}}) &= \delta_{Bx} + \delta_{Bx}\frac{\log\left|\cos\theta^{B_{\text{in}}}\right|}{\log r_3}\\ &= \delta_{Bx}\left(1 - \frac{1}{2}\frac{\log\left(1+\tan^2\theta^{A_{\text{in}}}\, x_2^{2(\delta_{Ay}-\delta_{Ax})}\right)}{\delta_A(\theta^{A_{\text{in}}})\log x_2}\right).\end{aligned}$$

Now, $\tan\theta^{C_{\text{in}}}$ is small compared to 1, since we are in the region where $\cot\theta^{B_{\text{in}}} \gg r_3^{\frac{\delta_{By}}{\delta_{Bx}}-1}$. This follows from noting that

$$\begin{aligned}\tan\theta^{C_{\text{in}}} &= \tan\theta^{B_{\text{in}}} r_3^{1-\frac{\delta_{Bx}}{\delta_{By}}}\left|\cos\theta^{B_{\text{in}}}\right|^{1-\frac{\delta_{Bx}}{\delta_{By}}}\\ &= \left|\tan\theta^{B_{\text{in}}} r_3^{\frac{\delta_{By}}{\delta_{Bx}}-1}\right|^{\frac{\delta_{Bx}}{\delta_{By}}}\left|\sin\theta^{B_{\text{in}}}\right|^{1-\frac{\delta_{Bx}}{\delta_{By}}}\operatorname{sgn}\left(\tan\theta^{B_{\text{in}}}\right).\end{aligned}$$

The first term is small by assumption, and the second and third are at most 1 since $\delta_{Bx} < \delta_{By}$ (assumption **A7**). Therefore we use the X part of the map at C, and get, after ϕ_C and Ψ_{CA}:

$$\log\hat{x}_2 = \log D_A + \delta_C(\theta^{A_{\text{in}}})\log x_1$$

where $\hat{x}_2$ is the value of x_2 on $\mathbf{H}_A^{\text{in}}$ after one full circuit of the network and

$$\begin{aligned}\delta_C(\theta^{A_{\text{in}}}) &= \delta_{CX} - \frac{c_{CX}-c_{CY}}{2\lambda\log x_1}\log\left(1-\tan^2\theta^{C_{\text{in}}}\right)\\ &= \delta_{CX} + \frac{c_{CX}-c_{CY}}{2\lambda\delta_A(\theta^{A_{\text{in}}})\delta_{Bx}\log x_2}\tan^2\theta^{C_{\text{in}}}\end{aligned}$$

since $\tan^2\theta^{C_{\rm in}} \ll 1$.

Substituting for x_1 in the above expression for $\hat{x}_2$, we find that

$$\log \hat{x}_2 = \log D_X + \delta(\theta^{A_{\rm in}}) \log x_2,$$

where

$$\log D_X \approx \log D_A(0) + \delta_{CX} \left(\log D_C(0) + \delta_{Bx} \log D_B(0)\right)$$

and

$$\begin{aligned}
\delta(\theta^{A_{\rm in}}) &= \delta_A(\theta^{A_{\rm in}})\delta_B(\theta^{A_{\rm in}})\delta_C(\theta^{A_{\rm in}}) \\
&= \delta_A(\theta^{A_{\rm in}})\delta_{Bx} \left(1 - \frac{1}{2}\frac{\log\left(1+\tan^2\theta^{A_{\rm in}}\, x_2^{2(\delta_{Ay}-\delta_{Ax})}\right)}{\delta_A(\theta^{A_{\rm in}})\log x_2}\right) \\
&\qquad \times \left(\delta_{CX} + \frac{c_{CX}-c_{CY}}{2\lambda\delta_A(\theta^{A_{\rm in}})\delta_{Bx}\log x_2}\tan^2\theta^{C_{\rm in}}\right) \\
&\approx \delta_{Bx}\delta_{CX}\left(\delta_A(\theta^{A_{\rm in}}) - \frac{1}{2}\frac{\log\left(1+\tan^2\theta^{A_{\rm in}}\, x_2^{2(\delta_{Ay}-\delta_{Ax})}\right)}{\log x_2}\right) \\
&= \delta_X + \delta_{Bx}\delta_{CX}\frac{\log\left|\cos\theta^{A_{\rm in}}\right|}{\log x_2}.
\end{aligned}$$

We have ignored the correction term in $\delta_C(\theta^{A_{\rm in}})$ since it is much smaller than that in $\delta_A(\theta^{A_{\rm in}})$.

In this region, $\delta(\theta^{A_{\rm in}})$ ranges between δ_X (when $\theta^{A_{\rm in}} = 0$) and $\delta_{Ay}\delta_{By}\delta_{CX}$, since at the edge of region 1, $\cos\theta^{A_{\rm in}} \sim x_2^{\frac{\delta_{By}}{\delta_{Bx}}\sigma}$.

Region 2. Now consider the region with $\tan\theta^{A_{\rm in}}\, x_2^{\frac{\delta_{By}}{\delta_{Bx}}\sigma} \gg 1$. Orbits with $\theta^{A_{\rm in}}$ in this region will visit the Y parts of all three maps. Note that since $\delta_{By} > \delta_{Bx}$, the above assumption also implies that $\tan\theta^{A_{\rm in}}\, x_2^{\delta_{Ay}-\delta_{Ax}} \gg 1$.

For ϕ_A in this region we write

$$\delta_A(\theta^{A_{\rm in}}) = \delta_{Ay} + \frac{\log\left|\sin\theta^{A_{\rm in}}\right|}{\log x_2} + \frac{1}{2}\frac{\log\left(1+\cot^2\theta^{A_{\rm in}}\, x_2^{2(\delta_{Ax}-\delta_{Ay})}\right)}{\log x_2},$$

and we can approximate $\delta_A(\theta^{A_{\rm in}})$ by δ_{Ay}.

After ϕ_B, we find

$$\begin{aligned}
\delta_B(\theta^{A_{\rm in}}) =& \delta_{By} + \delta_{By}\frac{\frac{1}{2}\cot^2\theta^{B_{\rm in}}\, r_3^{2(1-\frac{\delta_{By}}{\delta_{Bx}})}}{\log r_3} \\
=& \delta_{By}\left(1 + \frac{\frac{1}{2}\cot^2\theta^{A_{\rm in}}\, x_2^{-2\frac{\delta_{By}}{\delta_{Bx}}\sigma}}{\delta_{Ay}\log x_2}\right)
\end{aligned}$$

and after ϕ_C we find

$$\delta_C(\theta^{A_{\rm in}}) = \left(\delta_{CY} - \frac{c_{CX} - c_{CY}}{2\lambda\delta_{Ay}\delta_{By}\log x_2}\cot^2\theta^{A_{\rm in}}\, x_2^{-2\frac{\delta_{By}}{\delta_{Bx}}\sigma}\right).$$

The corrections to the B and C parts of the map are small and comparable, but large compared to the correction to the A part of the map, so we find, for $\tan\theta^{A_{\rm in}}\, x_2^{\frac{\delta_{By}}{\delta_{Bx}}\sigma} \gg 1$,

$$\delta(\theta^{A_{\rm in}}) = \delta_Y + \left(\delta_{By}\delta_{CY} + \frac{(\delta_{CY} - \delta_{CX})e_C}{\lambda}\right)\frac{\cot^2\theta^{A_{\rm in}}\, x_2^{-2\frac{\delta_{By}}{\delta_{Bx}}\sigma}}{2\log x_2}.$$

In this region, the correction term could be of either sign since $\delta_{CX} > \delta_{CY}$. However, in the limit of small x_2, the value of $\delta(\theta^{A_{\rm in}})$ in all of region 2 is δ_Y.

4.3. Case I: Resonance of a single subcycle. We can use the results derived in the previous section to consider resonance bifurcations of a distinguished subcycle within the Case I network. These results could be derived using the traditional cross-sections (as is done explicitly in [17]), and the results would be identical. However, rather than repeat that analysis, we show how these results can be achieved using our new methods. Specifically, we consider the subcycle of the network given by $A \to B \to X \to A$, which lies in the subspace $y_3 = 0$. This cycle cannot be asymptotically stable since B has a two-dimensional unstable manifold.

The dynamics near this cycle are described by a two-dimensional map. Using the results of the previous section, it can be shown that the return map starting on $\mathbf{H}^{\rm in}_A$ is given by

$$\begin{aligned} x_2 &\to D_X x_2^{\delta_X}, \\ \theta_3 &\to \theta_3 x_2^{\nu_{AX}}. \end{aligned}$$

If we start on a different section, the map will be similar, with, e.g., x_2 replaced by r_3, and ν_{AX} replaced by ν_{BY}.

The fixed point in this map at $\theta_3 = x_2 = 0$ corresponds to the heteroclinic cycle. We know the cycle cannot be asymptotically stable, but it can be attracting if $\delta_X > 1$ and $\nu_{AX} > 0$ (as discussed above).

A resonance bifurcation of the heteroclinic cycle occurs when $\delta_X = 1$. This bifurcation creates a fixed point of the map at $\theta_3 = 0$, $x_2 = D_X^{1/(1-\delta_X)}$, which is also in the subspace $y_3 = 0$. Furthermore, it is straightforward to show that if $0 < D_X < 1$ then a periodic orbit occurs for $\delta_X < 1$ and so the bifurcation is supercritical, while if $D_X > 1$ then a periodic orbit occurs when $\delta_X > 1$ and so the bifurcation is subcritical. If this bifurcation occurs supercritically, then the resulting periodic orbit will be asymptotically stable. That is, we have the possibility that the resonance bifurcation is from a heteroclinic cycle that is *not* asymptotically stable but it produces a periodic orbit that *is* asymptotically stable. To the best of our knowledge, this scenario has not been reported before.

4.4. Composing the maps: Case II. We repeat the above calculations for the network with complex eigenvalues. There are again two regions, given by the same conditions as before. Due to the rotation of θ_3 at A, the regions are defined on $\mathbf{H}_B^{\text{in}}$ rather than $\mathbf{H}_A^{\text{in}}$, but we could map these back to $\mathbf{H}_A^{\text{in}}$ using the expression $\theta^{B_{\text{in}}} = \theta^{A_{\text{in}}} - \frac{\omega}{e_A}\log x_2$.

We again begin by considering the θ_3 components of the maps at $\theta^{B_{\text{in}}} = 0$ and $\theta^{B_{\text{in}}} = \frac{\pi}{2}$. These points are not subspaces in this case (as they are in Case I), but can still give us information on the geometry of the θ_3 part of the return maps. The calculations proceed exactly as before, except that $c_{Ax} = c_{Ay} = c_A$. This means we have a simplification and find

$$\nu_{AX} = \delta_A\left(1 - \frac{\delta_{Bx}}{\delta_{By}}\right) + \frac{\lambda}{e_C}\delta_A\delta_{Bx}$$

which must be positive. The relationships with ν_{BX} and ν_{CX} given in section 4.2.1 imply that in addition $\nu_{BX} > 0$ and $\nu_{CX} > 0$. Thus the θ_3 part of the return map will have a small gradient close to the point where $\theta^{B_{\text{in}}} = 0$.

The computation of ν_{AY}, ν_{BY} and ν_{CY} follows as in Case I, and again we see that they all have the same sign so long as we are close enough to $\delta_Y = 1$. We assume that this is the case, and further, that they are all positive, as before. The dynamics in the case where $\nu_{AY} < 0$ is very similar. Thus, again, we need only consider the return map starting on $\mathbf{H}_A^{\text{in}}$.

The graph of $\hat{\theta}^{A_{\text{in}}}$ against $\theta^{A_{\text{in}}}$ will look very similar to that for Case I, shown in figure 4.1(a), except that as the initial value of x_2 varies, the graph will shift to the right or left. This is discussed in more detail in section 5.2.

We next compute $\delta(\theta^{A_{\text{in}}})$ for Case II, in exactly the same manner as for Case I. The only difference occurs after ϕ_A; now we have $\delta_A(\theta^{A_{\text{in}}}) = \delta_A$, which is a constant, and

$$\theta^{B_{\text{in}}} = \theta^{A_{\text{in}}} - \frac{\omega}{e_A}\log x_2.$$

The remainder of the calculations follow in exactly the same manner, and we find that in region 1,

$$\delta(\theta^{A_{\text{in}}}) = \delta_X + \delta_{Bx}\delta_{CX}\frac{\log\left|\cos\left(\theta^{A_{\text{in}}} - \dfrac{\omega}{e_A}\log x_2\right)\right|}{\log x_2}$$

and in region 2,

$$\delta(\theta^{A_{\text{in}}}) = \delta_Y + \left(\delta_{By}\delta_{CY} + \frac{(\delta_{CY} - \delta_{CX})e_C}{\lambda}\right)\frac{\cot^2\left(\theta^{A_{\text{in}}} - \frac{\omega}{e_A}\log x_2\right)\, x_2^{2\delta_A(1-\frac{\delta_{By}}{\delta_{Bx}})}}{2\log x_2}.$$

5. Resonance of heteroclinic networks. We are now in a position to determine the effect on the dynamics near each network of one or more of the cycles within

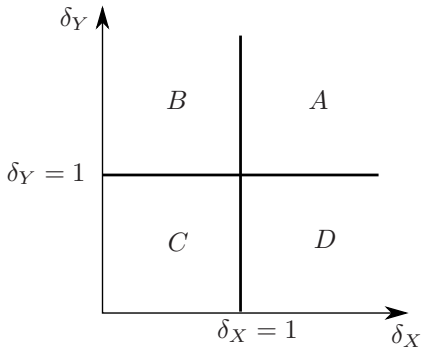

FIG. 5.1. *The (δ_X, δ_Y) parameter plane, showing the definition of the quadrants A, B, C, and D.*

the network undergoing a resonance bifurcation. We focus on finding fixed points of the approximate return maps we have derived, which correspond to periodic orbits that make one circuit of the network before closing.

Throughout this section, we start with a circle of initial conditions on $\mathbf{H}_A^{\text{in}}$ with fixed x_2 and $0 \leq \theta_3 < 2\pi$, and consider the values of x_2 and θ_3 when these trajectories first return to $\mathbf{H}_A^{\text{in}}$; we again refer to these values as $\hat{x}_2$ and $\hat{\theta}_3$, respectively. We use the approximations for the maps derived in section 4.1 to plot 'nullclines' of θ_3 and x_2 on $\mathbf{H}_A^{\text{in}}$. A point $(\theta_3, x_2) \in \mathbf{H}_A^{\text{in}}$ is said to be on the x_2-nullcline (resp. θ_3-nullcline) if the value of x_2 (resp. θ_3) after one circuit around the network is unchanged (resp. unchanged modulo 2π). Fixed points of the Poincaré map occur when the x_2- and θ_3-nullclines cross. We can identify these from the sketches of the nullclines, and are also able in some cases to identify the stability of the fixed points by considering how x_2 and θ_3 vary close to the fixed points.

We then discuss how the nullcline figures change as the quantities δ_X and δ_Y are varied and are thus able to draw bifurcation diagrams. Figure 5.1 shows the (δ_X, δ_Y) parameter plane, and labels the four quadrants around the point $\delta_X = \delta_Y = 1$. In the following, we refer to these quadrants and also draw bifurcation diagrams as we traverse a small circle around the point $\delta_X = \delta_Y = 1$.

Recall that for both networks the return map has the general form

$$\log \hat{x}_2 = \log D(\theta_3) + \delta(\theta_3) \log x_2 \tag{5.1}$$

where $D(\theta_3)$ is the constant arising from the global parts of the map and $\delta(\theta_3)$ (which depends on x_2 as well as θ_3) was calculated in section 4. If $\delta(\theta_3) > 1$ for all θ_3 and $D(\theta_3) < 1$ for all θ_3, then $\log \hat{x}_2 < \log x_2$ for all θ_3 and all small x_2. Hence, the network is asymptotically stable. If $\delta(\theta_3) > 1$ but $D(\theta_3) > 1$ for some θ_3, then for sufficiently small x_2, $\log \hat{x}_2 < \log x_2$ and the network is still asymptotically stable. However, if $D(\theta_3) > 1$ and x_2 is large enough that $\log x_2 > \log D(\theta_3)/(1 - \delta(\theta_3))$, then $\log \hat{x}_2 > \log x_2$ and trajectories move away from the network. Thus, in the case that $D(\theta_3) > 1$ for some θ_3, the basin of attraction of the network could be quite small as $\delta(\theta_3) \to 1$ from above.

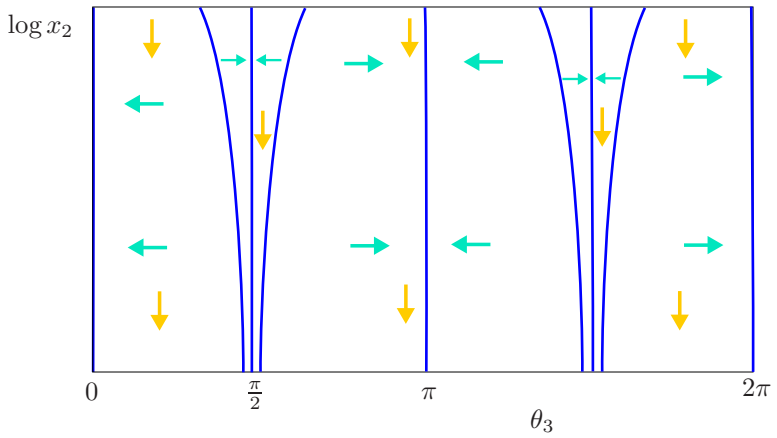

FIG. 5.2. *The figure shows θ_3-nullclines on $\mathbf{H}_A^{\text{in}}$ (in blue) for the network in Case I, when $\nu_{AX} > 0$, and $\delta(\theta_3) > 1$, so the network is attracting (quadrant A in figure 5.1). The orange arrows indicate that x_2 is decreasing, and the blue arrows indicate the direction of change of θ_3.*

For simplicity, we thus consider only the case when $D(\theta_3) < 1$ for all θ_3. This means the network is attracting and has a large basin of attraction if $\delta(\theta_3) > 1$ for all θ_3, which makes it simpler to study what happens when $\delta(\theta_3)$ goes through 1. This condition on $D(\theta_3)$ is similar to assuming a supercritical bifurcation in other types of bifurcation.

5.1. Case I: Computing nullclines. We first consider computing the θ_3 and x_2 nullclines for Case I, the network with real eigenvalues.

5.1.1. θ_3-nullclines. We begin by finding fixed points of the θ_3 part of the map, and using this information to draw θ_3-nullclines on $\mathbf{H}_A^{\text{in}}$. Figure 4.1 shows the value of θ_3 after one excursion around the network. There are fixed points at $\theta_3 = 0$, $\frac{\pi}{2}$, π, $\frac{3\pi}{2}$. If $\nu_{AY} > 0$, then there are four further fixed points either side of $\frac{\pi}{2}$ and $\frac{3\pi}{2}$. These additional points are at (approximately) $\frac{\pi}{2} \pm \theta^{\epsilon_A}$ and $\frac{3\pi}{2} \pm \theta^{\epsilon_A}$, and so get closer to $\frac{\pi}{2}$ and $\frac{3\pi}{2}$ as x_2 decreases.

Figure 5.2 shows a sketch of the θ_3-nullclines in the case $\nu_{AY} > 0$. The distance from the curved θ-nullclines to $\frac{\pi}{2}$ scales like $x_2^{\frac{\delta_{By}}{\delta_{Bx}}\sigma}$. The blue arrows in the figure indicate how θ_3 changes under iteration of the map. This shows that the nullclines at $\theta_3 = 0$, $\frac{\pi}{2}$, π, $\frac{3\pi}{2}$ are attracting, but the additional (curved) nullclines are repelling. In the case that $\nu_{AY} < 0$, the additional nullclines are not present and the nullclines at $\frac{\pi}{2}$ and $\frac{3\pi}{2}$ are repelling.

5.1.2. x_2-nullclines. We next construct the x_2-nullclines. Our calculations are done explicitly for the region $0 \leq \theta_3 \leq \frac{\pi}{2}$ but results for the remaining values of θ_3 follow from symmetry.

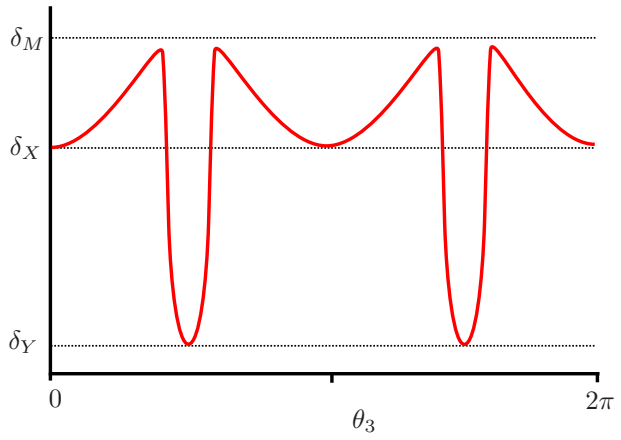

FIG. 5.3. *Case I: a sketch of $\delta(\theta_3)$ against θ_3 for fixed x_2.*

The return map has the form given in (5.1) with

$$\delta(\theta_3) = \begin{cases} \delta_X + \delta_{Bx}\delta_{CX}\dfrac{\log|\cos\theta_3|}{\log x_2} & 0 < \theta_3 < \frac{\pi}{2} - \theta^{\epsilon_A}, \\ \delta_Y + \left(\delta_{By}\delta_{CY} + \dfrac{(\delta_{CY} - \delta_{CX})e_C}{\lambda}\right)\dfrac{\cot^2\theta_3\, x_2^{-2\frac{\delta_{By}}{\delta_{Bx}}\sigma}}{2\log x_2} & \frac{\pi}{2} - \theta^{\epsilon_A} < \theta_3 \le \frac{\pi}{2}. \end{cases}$$

Figure 5.3 shows a sketch of $\delta(\theta_3)$ against θ_3. As discussed in section 4.1, in region 1, $\delta(\theta_3)$ varies between δ_X and δ_M, where $\delta_M = \delta_{Ay}\delta_{By}\delta_{CX}$. Note that δ_M is greater than both δ_X (since $\sigma > 0$ implies that $\delta_{Ay}\delta_{By} > \delta_{Ax}\delta_{Bx}$) and δ_Y (since $\delta_{CX} > \delta_{CY}$). The existence of this maximum of $\delta(\theta_3)$ close to δ_M is persistent in the limit of small x_2. Note also that $\theta_3 = 0,\ \pi$ are always local minima of $\delta(\theta_3)$ but $\theta_3 = \frac{\pi}{2},\ \frac{3\pi}{2}$ could be local minima or maxima, depending on the sign of the factor in front of the second term in $\delta(\theta_3)$ in region 2. However, this correction term is much smaller than the correction term to $\delta(\theta_3)$ in region 1, and the value of $\delta(\theta_3)$ on the boundary of region 2 tends to δ_Y in the limit of small x_2.

Thus, the maximum value of $\delta(\theta_3)$ is δ_M, and the minimum, in the limit of small x_2, is either δ_X or δ_Y. In [18], we showed that if $\min_{\theta_3}\delta(\theta_3) > 1$, then the heteroclinic network is asymptotically stable, and if $\max_{\theta_3}\delta(\theta_3) < 1$, then the heteroclinic network is completely unstable in that the basin of attraction has measure zero. Therefore, we expect to see stability changes, or resonances, of the heteroclinic network when δ_X, δ_Y or δ_M pass through 1.

Intuitively, we expect to find fixed points near $\theta_3 = 0$ if $\delta_X < 1$ (but close to one) and fixed points near $\theta_3 = \frac{\pi}{2}$ if $\delta_Y < 1$ (but close to one). To check this, we find the x_2-nullclines explicitly by finding solutions to the equation

$$\log x_2 = \log D(\theta_3) + \delta(\theta_3)\log x_2.$$

If such solutions exist in the region $\theta < \frac{\pi}{2} - \theta^{\epsilon_A}$, then we have

$$\log x_2 = \log D(\theta_3) + \delta_X \log x_2 + \delta_{Bx}\delta_{CX} \log|\cos\theta_3|$$

which, after rearranging gives the curve describing the nullclines:

$$\log x_2 = \frac{1}{1-\delta_X}\left(\log D(\theta_3) + \delta_{Bx}\delta_{CX} \log|\cos\theta_3|\right).$$

Since we assume $D(\theta_3) < 1$, we require $\delta_X < 1$ for solutions in this region, as expected. This curve has a maximum at $\theta_3 = 0$, where $\log x_2 = \log D_X/(1-\delta_X)$. For later convenience, we define $x_X^\star = D_X^{1/(1-\delta_X)}$.

Suppose now that solutions exist in the region $\frac{\pi}{2} - \theta^{\epsilon_A} < \theta_3 < \frac{\pi}{2}$. These solutions satisfy

$$\log x_2 = \log D(\theta_3) + \delta_Y \log x_2 + \left(\delta_{By}\delta_{CY} + \frac{(\delta_{CY} - \delta_{CX})e_C}{\lambda}\right) \frac{\cot^2\theta_3\, x_2^{-2\frac{\delta_{By}}{\delta_{Bx}}\sigma}}{2\log x_2}.$$

To leading order, we can write this as

$$\log x_2 = \frac{1}{1-\delta_Y}\log D_Y,$$

and hence for solutions in this region we require $\delta_Y < 1$, as expected. For later use, we define $x_Y^\star = D_Y^{1/(1-\delta_Y)}$.

If $\delta_Y < 1$ and $\delta_M > 1$, then there will be additional solutions at the boundary of the two regions, that is, where $\theta_3 \sim \frac{\pi}{2} - \theta^{\epsilon_A}$, for $x_2 < x_Y^\star$. Note that the x_2-nullclines concerned have the same scaling (in terms of distance from $\frac{\pi}{2}$) as the additional θ_3-nullclines (which exist only if $\nu_{AY} > 0$). Thus, to determine the relative positions of the two sets of nullclines, and to work out where the nullclines cross, we would have to include more details about the global constants. In practice, it is likely that both cases are possible; we discuss the possibilities further below.

In figures 5.4, 5.5 and 5.6 we show sketches of the θ_3- and x_2-nullclines in the quadrants B, D and C around the point $\delta_X = \delta_Y = 1$, sufficiently close to that point so that $\delta_M > 1$. We show figures only for the case $\nu_{AY} > 0$, and so the additional x_2-nullclines are present, but discuss the case $\nu_{AY} < 0$ below.

In figure 5.4, $\delta_X < 1$ and $\delta_Y > 1$, and we can see that a stable fixed point occurs at $\theta_3 = 0$, $x_2 = x_X^\star$ (and similarly at $\theta_3 = \pi$, by symmetry). In figure 5.6, $\delta_Y < 1$ and $\delta_X > 1$. In the case shown, $\nu_{AY} > 0$, and there is the possibility of either one or three fixed points appearing close to $\theta_3 = \frac{\pi}{2}$ at resonance (and also near $\frac{3\pi}{2}$, by symmetry). The figure shows the case where the additional x_2-nullclines lie further from $\frac{\pi}{2}$ than the additional θ_3-nullclines, and three fixed points are created, one stable and two of saddle type. A second possibility is that the x_2-nullclines lie closer to $\frac{\pi}{2}$ than the θ_3-nullclines and there is only a single stable fixed point created as δ_Y passes through 1. If $\nu_{AY} < 0$, then there would also only be a single fixed point created as

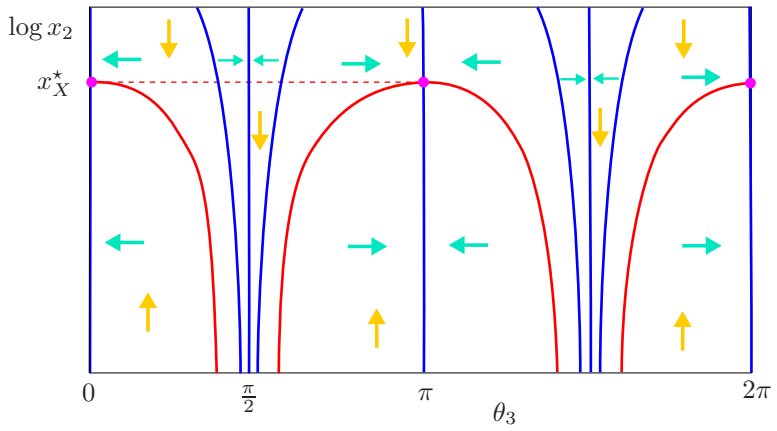

FIG. 5.4. *The figure shows nullclines on* $\mathbf{H}_A^{\text{in}}$ *for* θ_3 *(blue) and* x_2 *(red) for Case I, in quadrant B of the* (δ_X, δ_Y)*-plane. The orange and blue arrows denote the direction of change of* x_2 *and* θ_3 *respectively. The pink dots indicate stable fixed points of the map.*

δ_Y decreases through 1, but in this case it would be of saddle type as the nullcline at $\theta_3 = \frac{\pi}{2}$ would be repelling.

In figure 5.5, $\delta_X, \delta_Y < 1$, and we show the figure for $\delta_M > 1$. Both sets of fixed points described above exist, and all the nullclines continue to exist as $\log x_2$ decreases to $-\infty$. In this case, the fixed points created in the two resonance bifurcations at $\delta_X = 1$ or $\delta_Y = 1$ do not interact with each other, a consequence of the two red nullclines being distinct from one another for arbitrarily small x_2.

Finally, in figure 5.7 we show the case where $\delta_M < 1$. This is still in quadrant C of the (δ_X, δ_Y) plane, since $\delta_M > \delta_X, \delta_Y$. In this case the x_2-nullclines created in the two resonance bifurcations of the individual sub-cycles have joined up, and x_2-nullclines exist only for a finite range of $\log x_2$. The additional resonance bifurcation that occurs when δ_M passes through 1 has the possibility of creating further fixed points near the additional θ_3-nullclines, if they exist (i.e., if $\nu_{AY} > 0$), and if they were not already created in the $\delta_Y = 1$ resonance.

5.1.3. Bifurcation diagrams. We now use the nullcline sketches to draw bifurcation diagrams. In figure 5.8 we show a bifurcation diagram obtained as a circle is traversed around the point $\delta_X = \delta_Y = 1$ in the (δ_X, δ_Y) plane. We assume we are close enough to this point so that $\delta_M > 1$ and hence that the periodic orbits created when δ_X passes through one are not connected to those that arise when δ_Y passes through one.

If $\nu_{AY} > 0$, there are two cases to consider: either the x_2-nullclines are closer to $\frac{\pi}{2}$ or further from $\frac{\pi}{2}$ than the curved θ_3-nullclines. In the first case, the only equilibria are at $\theta_3 = 0$ and $\theta_3 = \frac{\pi}{2}$. In the second case, there will be further equilibria; one possibility is shown in the right panel of figure 5.8.

The supplementary online material contains a movie showing how the nullclines in

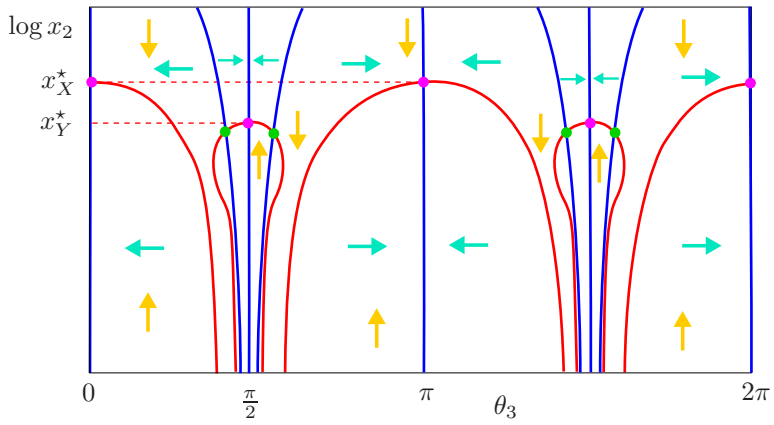

FIG. 5.5. *The figure shows nullclines on* $\mathbf{H}_A^{\text{in}}$ *for* θ_3 *(blue) and* x_2 *(red) for Case I, in quadrant C of the* (δ_X, δ_Y) *plane. All lines, curves and dots have the same interpretation as in figures 5.4 except that the green dots indicate saddle fixed points.*

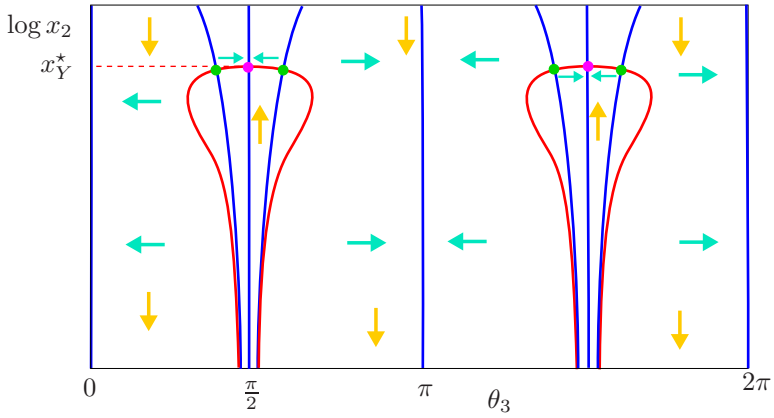

FIG. 5.6. *The figure shows nullclines on* $\mathbf{H}_A^{\text{in}}$ *for* θ_3 *(blue) and* x_2 *(red) for Case I, in quadrant D of the* (δ_X, δ_Y) *plane, in the case* $\delta_M > 1$ *All lines, curves and dots have the same interpretation as in figures 5.4 and 5.5.*

Case I vary as a circle of radius 0.02 around $\delta_X = \delta_Y = 1$ is traversed in the (δ_X, δ_Y) plane. In this movie, we kept σ fixed at 0.05, $\frac{\lambda}{e_C} = 0.07$, $\frac{\delta_{Bx}}{\delta_{By}} = 0.93$, $\frac{\delta_{CX}}{\delta_{CY}} = 1.08$, and chose the other coefficients such that the value of $\frac{\lambda}{e_C}$ for which $\delta(\frac{\pi}{2})$ changes from a local minimum to a local maximum is 0.07. The red solid curves are the small nullclines in region 1, the green solid curves are the small nullclines in region 2, and the blue solid curves are the θ_3 nullclines. The red and green dashed curves are the approximate small nullclines computed above. Regions 1 and 2 are separated by green dashed curves. As the point $\delta_X = \delta_Y = 1$ is circled, the region 1 and region 2 small nullclines appear and disappear as the lines $\delta_X = 1$ and $\delta_Y = 1$ are crossed respectively, leading to the creation or destruction of fixed points near X or Y.

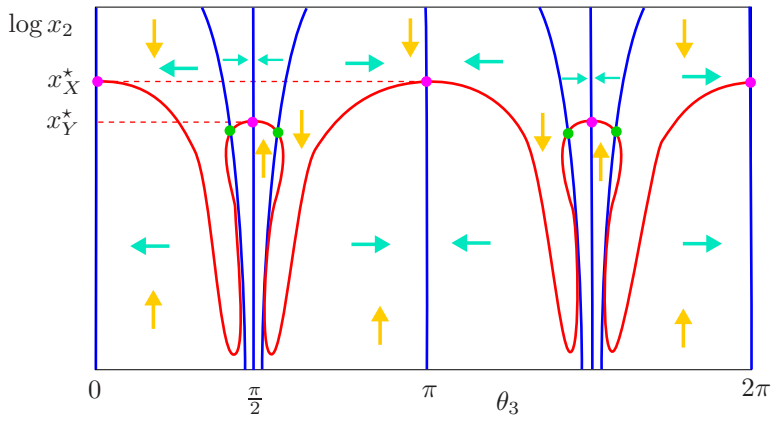

FIG. 5.7. *The figure shows nullclines on* $\mathbf{H}_A^{\text{in}}$ *for* θ_3 *(blue) and* x_2 *(red) for Case I, in quadrant C of the* (δ_X, δ_Y) *plane, in the case* $\delta_M < 1$*. All lines, curves and dots have the same interpretation as in figures 5.4 and 5.5.*

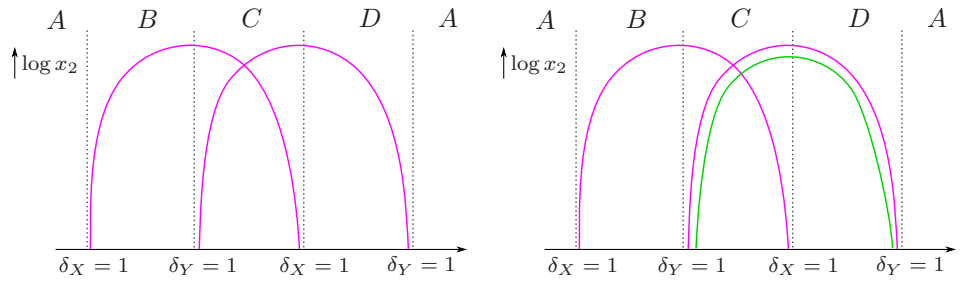

FIG. 5.8. *The figures show the creation of periodic orbits as a circle is traversed clockwise in* (δ_X, δ_Y) *space around the point* $\delta_X = \delta_Y = 1$*, for the Case I network. The left hand figure shows the case when the* x_2*-nullclines are inside the curved* θ_3*-nullclines, and the right hand figure shows the case when the* x_2*-nullclines are outside these* θ_3*-nullclines. The labels A, B, C and D correspond to the quadrants labelled in figure 5.1. The pink curves indicate stable periodic orbits and the green curves indicate saddle periodic orbits. (Note that the pink curve actually represents two symmetry-related orbits and the green curve four).*

5.2. Case II: constructing nullclines. A similar analysis can be performed for the network with complex eigenvalues.

5.2.1. θ_3**-nullclines.** We will assume that $\nu_{AY} > 0$; the situation for $\nu_{AY} < 0$ in Case II has only very minor differences.

Plotting the value of $\hat{\theta}_3$ as a function of θ_3 for some fixed initial value of x_2 gives a schematic picture similar to that shown in figure 4.1(a). However, differences are noticed as the value of x_2 is decreased. Specifically, the effects of reducing the initial value of x_2 include those given above for Case I, i.e., the steep portions of the graphs become steeper, and the small 'step' becomes smaller, but the additional time spent in a neighbourhood of A when x_2 is smaller means that the value of θ_3 is 'rotated' for longer due to the complex eigenvalues (specifically, $\theta^{B_{\text{in}}} = \theta^{A_{\text{in}}} - \frac{\omega}{e_A} \log x_2$). This has the effect of shifting the graph of $\hat{\theta}_3$ to the left as x_2 is decreased. This means that

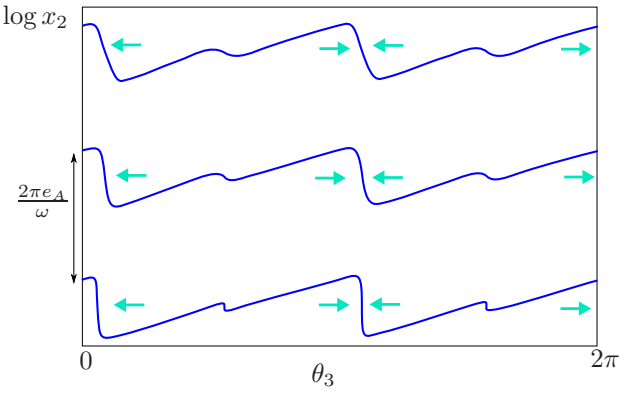

FIG. 5.9. *Case II: nullclines of θ_3 (blue curves). Compare with figure 4.1 which shows how θ_3 varies at fixed x_2. The blue arrows indicate the direction of change of θ.*

the topology of the θ_3-nullclines is different in Cases I and II, as we now explain.

For the value of x_2 shown in figure 4.1, there are four points at which the value of θ_3 is the same after one circuit of the network. These points are thus on the θ_3-nullclines. As x_2 decreases, the graph of $\hat{\theta}_3$ moves to the left, and thus the four 'fixed points' in the θ_3 map come together and disappear in pairs, in a manner similar to a saddle-node bifurcation in a map. There are then some values of x_2 for which there are no fixed points in the θ_3 map. If x_2 decreases so that the value of $\theta_3 - \frac{\omega}{e_A}\log x_2$ has changed by 2π, then the graph in 4.1 will have rotated back to its original position (except that since x_2 will now have decreased, the vertical parts will be steeper and the small step smaller, as discussed previously).

Figure 5.9 shows the location of the θ_3-nullclines on $\mathbf{H}_A^{\text{in}}$. The vertical gap between the nullclines is such that the difference in $\log x_2$ is $\frac{2\pi e_A}{\omega}$. Note that $\mathbf{H}_A^{\text{in}}$ is a cylinder, and each of the θ_3-nullclines is topologically a circle around the cyclinder. There is an infinite number of these nullclines. The larger approximately vertical portions of each θ_3-nullcline should appear at $\theta_3 = 0$ and $\theta_3 = \pi$, by our assumption that the global parts of the θ_3 maps do nothing. However, for clarity, in this and following figures we show these portions of the curves slightly away from 0 and π. This has no effect on the topology of the intersections of the θ_3-nullclines with the x_2-nullclines we describe later.

In figure 5.9 we also show how θ_3 changes away from the nullclines, marked with blue arrows. We only include these close to the nullclines, as since θ_3 is a circular variable, it does not make sense to say whether θ_3 is increasing or decreasing when it is changing by a large amount. Thus the direction of change of θ_3 can change from right to left without crossing a nullcline.

5.2.2. x_2-nullclines. Determination of the existence and shape of the x_2-nullclines proceeds exactly as in Case I, except for consideration of additional rotation as x_2 decreases, as for the θ_3-nullclines. Thus, the x_2-nullclines for Case II will look the

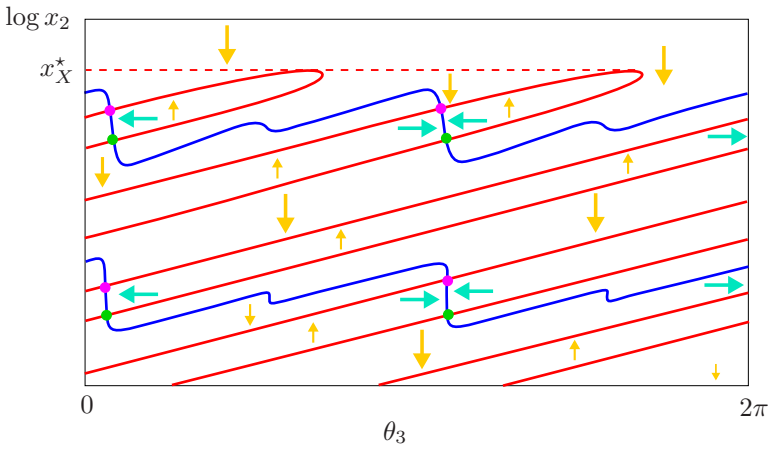

FIG. 5.10. *Case II with $\delta_Y > 1 > \delta_X$ (quadrant B): nullclines for θ_3 (blue) and x_2 (red). Pink and green dots mark fixed points; their stabilities are discussed in the text. The orange and blue arrows denote the direction of change of x_2 and θ_3 respectively.*

same as in Case I except that the θ_3 coordinate is replaced by $\theta_3 - \frac{\omega}{e_A}\log x_2$. In other words, the θ_3 coordinate of the nullclines rotates to the left as x_2 decreases.

Figures 5.10, 5.11, and 5.12 show the θ_3 and x_2-nullclines for quadrants B, C and D of the (δ_X, δ_Y) plane respectively, for $\delta_M > 1$. In these cases, the x_2-nullclines exist for arbitrarily small x_2, and so there will be an infinite number of intersections of the θ_3- and x_2-nullclines, and hence an infinite number of fixed points in the map or periodic orbits in the original flow.

In figure 5.10, $\delta_X < 1$ and $\delta_Y > 1$. As δ_X decreases through 1, fixed points are created in saddle-node bifurcations for $\theta_3 \approx 0, \pi$ and with $x_2 \approx x_X^\star$. In each saddle-node pair, the larger amplitude solution is initially stable, and the smaller is of saddle-type. As δ_X changes, it is likely that these fixed points undergo period-doubling or other types of bifurcation, and hence their stabilities may change.

In figure 5.12, $\delta_Y < 1$ and $\delta_X > 1$. As δ_Y decreases through 1, fixed points are now created in saddle-node pairs near $\theta_3 \approx \frac{\pi}{2}, \frac{3\pi}{2}$ and with $x_2 \approx x_Y^\star$. Again these fixed points will initially be created in stable-saddle pairs, but due to the small step in the θ_3 map and the shape of the θ_3-nullcline, we expect the θ_3 coordinate of these points to change rapidly as δ_Y is varied, and expect some of them to undergo stability changes too.

Figure 5.11 shows the situation when $\delta_X, \delta_Y < 1$, $\delta_M > 1$; as in Case I, sets of periodic orbits from the resonances at $\delta_X = 1$ and $\delta_Y = 1$ co-exist in this quadrant. Finally, in figure 5.13, we show the case $\delta_M < 1$. Here the x_2-nullclines only exist for a finite region of $\log x_2$, and hence there are only finitely many fixed points. Thus, the resonance bifurcation which occurs at $\delta_M = 1$ in the complex case results in the disappearance of infinitely many periodic orbits.

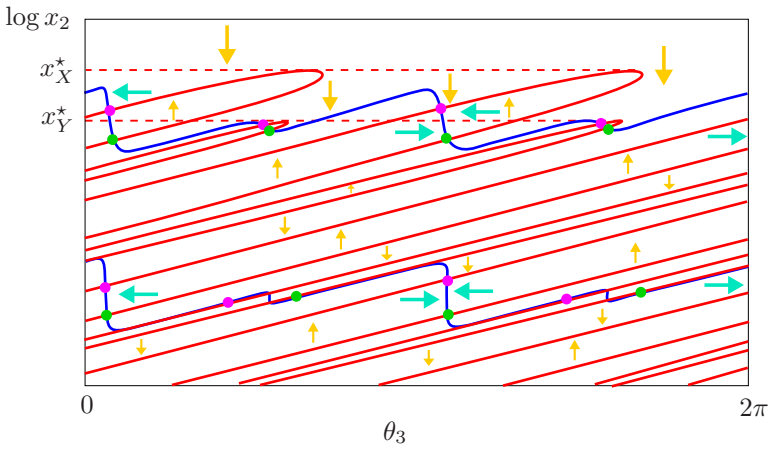

FIG. 5.11. *Case II with $\delta_Y < 1$, $\delta_X < 1$ (quadrant C), and with $\delta_M > 1$: nullclines for θ_3 (blue) and x_2 (red). Dots and arrows have the same meaning as in figure 5.10.*

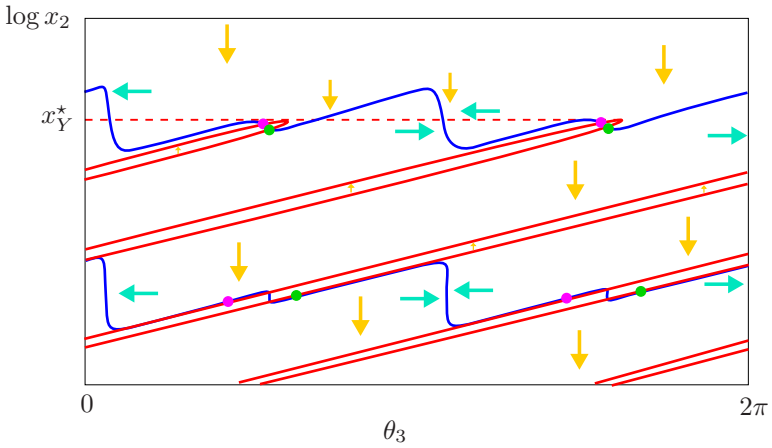

FIG. 5.12. *Case II with $\delta_X > 1 > \delta_X$ (quadrant D): nullclines for θ_3 (blue) and x_2 (red). Dots and arrows have the same meaning as in figure 5.10.*

5.2.3. Bifurcation diagrams. Figure 5.14 is a bifurcation diagram showing how periodic orbits are created and destroyed as a circle is traversed around the point $\delta_X = \delta_Y = 1$, assuming that $\delta_M > 1$.

The supplementary online material contains a movie showing how the nullclines in Case II vary as a circle of radius 0.02 around $\delta_X = \delta_Y = 1$ is traversed in the (δ_X, δ_Y) plane. In this movie, we kept σ fixed at 0.05, $\frac{\lambda}{e_C} = 0.07$, $\frac{\delta_{Bx}}{\delta_{By}} = 0.93$, $\frac{\omega}{e_A} = 0.5$, and chose the other coefficients such that the value of $\frac{\lambda}{e_C}$ for which $\delta(\frac{\pi}{2})$ changes from a local minimum to a local maximum is 0.07. The red solid curves are the small nullclines in region 1, the green solid curves are the small nullclines in region 2, and the blue solid curves are the θ_3 nullclines. Regions 1 and 2 are separated by green dashed curves. As the point $\delta_X = \delta_Y = 1$ is circled, the region 1 and region 2 small nullclines appear and disappear as the lines $\delta_X = 1$ and $\delta_Y = 1$ are crossed respectively, leading

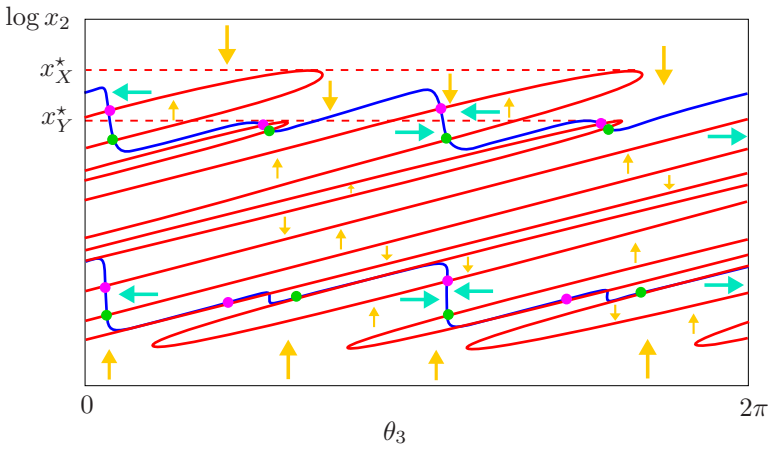

FIG. 5.13. *Case II with $\delta_Y < 1$, $\delta_X < 1$ (quadrant C), and with $\delta_M < 1$: nullclines for θ_3 (blue) and x_2 (red). Dots and arrows have the same meaning as in figure 5.10.*

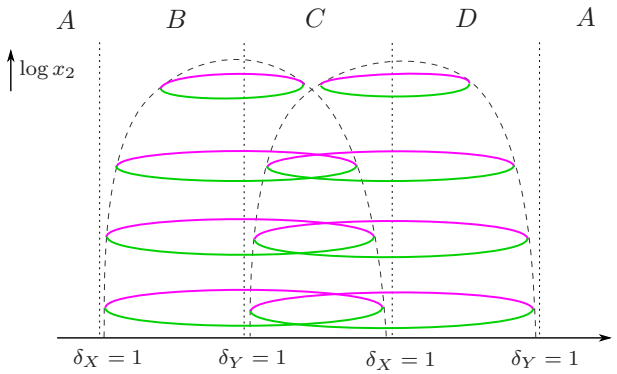

FIG. 5.14. *Case II: bifurcation diagram, showing the creation of periodic orbits as a circle is traversed clockwise around the point $\delta_X = \delta_Y = 1$ in (δ_X, δ_Y) space, where $\delta_M > 1$ on the entire circle. The labels A, B, C and D correspond to the quadrants shown in figure 5.1. The pink and green curves correspond to the fixed points coloured pink and green in figures 5.10-5.12; stabilities may change along these curves.*

to the creation or destruction of infinite numbers of fixed points.

5.2.4. Chaotic attractor. It was noted in [18] that chaotic attractors can be found close to the Case II network when $\delta_X < 1$ and $\delta_Y > 1$; it was argued that trajectories passing near X would be pushed away from the network (since $\delta_X < 1$) while trajectories passing near Y would be pulled towards the network (since $\delta_Y > 1$). A balance between contraction and expansion for orbits that pass repeatedly near X and Y could then be achieved, and may result in chaotic dynamics.

Here we refine this argument, supposing first that we have a chaotic attractor, and then looking more carefully at the conditions needed to allow it to exist. This hypothesized chaotic attractor will have a range of values of $\log x_2$ on $\mathbf{H}_A^{\text{in}}$, and so there will be a corresponding range of values of $\theta^{A_{\text{out}}} = \theta^{A_{\text{in}}} - \frac{\omega}{e_A} \log x_2$. If the

chaotic attractor is close to the network, then the range of $\theta^{A_{\text{out}}}$ will exceed 2π, and could be many times 2π. In this case, orbits on the attractor will experience an overall contraction (towards the network) that is the average of $\delta(\theta^{A_{\text{in}}})$, as given in section 4.4. We can approximate the average as:

$$\bar{\delta} = \frac{2}{\pi}\int_0^{\frac{\pi}{2}} \delta(\theta)\, d\theta \approx \delta_X + \frac{\delta_{Bx}\delta_{CX}}{\log x_2}\frac{2}{\pi}\int_0^{\frac{\pi}{2}} \log\cos\theta\, d\theta + \frac{\overline{\log D}}{\log x_2}.$$

Note the inclusion of $\overline{\log D}$ (the average of the global constant) in this expression. The contribution from the Y part of the cycle will be proportional to $x_2^{\frac{\delta_{By}}{\delta_{Bx}}\sigma}$, which is small compared to the $1/\log x_2$ term, and so has been dropped. The integral evaluates to $-\frac{\pi}{2}\log 2$, so we find

$$\bar{\delta} \approx \delta_X + \frac{\overline{\log D} - \delta_{Bx}\delta_{CX}\log 2}{\log x_2}.$$

Finding x_2 so that $\bar{\delta} = 1$ gives the expected distance of the chaotic attractor from the network:

$$\log x_2 \approx \frac{\overline{\log D} - \delta_{Bx}\delta_{CX}\log 2}{1-\delta_X} \tag{5.2}$$

suggesting that the chaotic attractor bifurcates from the network at $\delta_X = 1$ in the same way as the periodic orbits shown in figure 5.10. The term $-\delta_{Bx}\delta_{CX}\log 2$ is negative, which suggests that the chaotic attractor will be closer to the network than the periodic orbits. This issue is explored numerically in more detail below.

Replacing the actual trajectory by the average in this way implicitly assumes that the distribtution of $\theta^{A_{\text{out}}}$ is uniform. This will be a better approximation if the chaotic attractor is closer to the network, or if ω is larger. However, a non-uniform distribution would just lead to replacing $\log 2$ by a different order-one number.

Note that this estimate for the location of the chaotic attractor created in the $\delta_X = 1$ resonance is independent of δ_Y, in contrast to the explanation offered in [18].

5.2.5. Numerical example. In this section we give an ODE that has a network of the type we are considering in this article. We give an example close to $\delta_X = \delta_Y = 1$ where there are a large number of stable periodic orbits coexisting with three chaotic attractors at the same parameter values. The equations are similar to those presented in [18]:

$$\begin{aligned}
\dot{x}_1 &= x_1(1 - x_1^2 - 2x_2^2),\\
\dot{x}_2 &= x_2(1 - x_2^2 - (1+\delta_{CX})x_3^2 - (1+\delta_{CY})y_3^2),\\
\dot{x}_3 &= x_3\left(1 - (1+\delta_A)x_1^2 + \left(\frac{1-\delta_{Bx}}{\delta_{Bx}}\right)x_2^2 - x_3^2 - (1+\lambda)y_3^2\right) - \omega y_3 x_1^2,\\
\dot{y}_3 &= y_3\left(1 - (1+\delta_A)x_1^2 + \left(\frac{1-\delta_{By}}{\delta_{By}}\right)x_2^2 - (1+\lambda)x_3^2 - y_3^2\right) + \omega x_3 x_1^2.
\end{aligned}$$

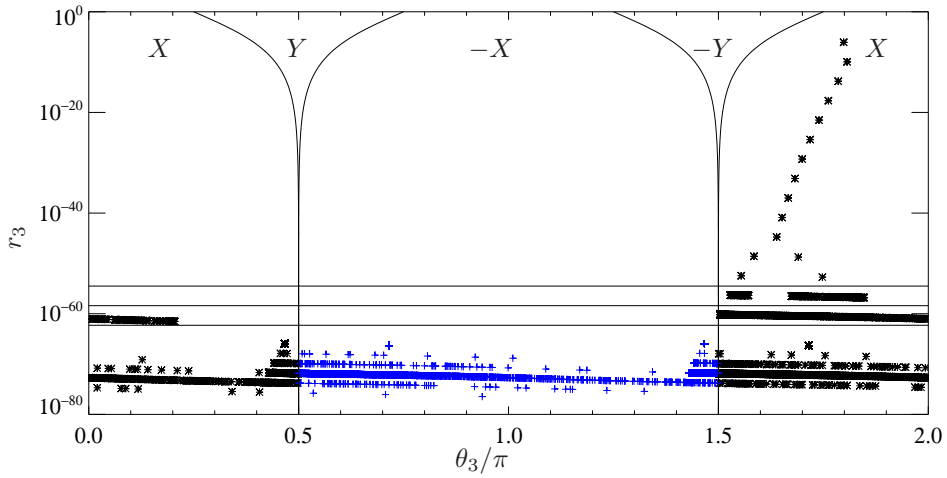

FIG. 5.15. *Intersection of* 16 *different trajectories with the Poincaré section* $\mathbf{H}_B^{\text{in}}$ *(*$h = 0.01$*), with* $\delta_X = \delta_Y = 0.99$*. Reading from the top down, there are* 11 *stable periodic orbits, each separated in logarithm by* $\frac{2\pi\epsilon_A}{\omega}$*. Next, there are two period-doubled periodic orbits, then (between the horizontal lines) there are two distinct regions of chaos that visit only* $+X$*. Below the third horizontal line there is a third region of chaos that extends to* $-X$ *as well; the average value of* $\log r_3$ *on this chaotic attractor is* -166 *(the average value of* $\log x_2$ *on* $\mathbf{H}_A^{\text{in}}$ *is* -230*). Black asterixes (blue plusses) indicate that the trajectory visits* X *(*$-X$*) immediately after leaving the Poincaré section. The boundaries of the cuspoidal regions are* $\tan\theta_3 = r_3^{1-\frac{\delta_{By}}{\delta_{Bx}}}$*; inside these cusps, trajectories would visit* Y *or* $-Y$*.*

These ODEs have the fixed points A at $(1,0,0,0)$, B at $(0,1,0,0)$, X at $(0,0,1,0)$ and Y at $(0,0,0,1)$. The constants δ_A, δ_{Bx}, etc. are eigenvalue ratios with the same meaning as used throughout this article.

We have carried out computations in each of the four quadrants indicated in figure 5.1, but present only one example here, for $\delta_X = \delta_Y = 0.99$ (quadrant C in the (δ_X, δ_Y) plane). The other parameters are $\delta_A = 0.7143$, $\delta_{Bx} = 1.4$, $\delta_{By} = 1.5054$, $\delta_{CX} = 0.99$, $\delta_{CY} = 0.9207$, $\lambda = 0.07$ and $\omega = 0.5$. The combination δ_M is 1.0645, σ is 0.05, and all the ν's are positive. The numerical methods are as described in [18].

In this example, the network is unstable and trajectories that start very close to the network move away from it. We have found 11 stable periodic orbits in the locations that would be expected from the considerations in section 5.2.2. Closer to the network than these, there are two period-doubled orbits and three distinct regions of chaos. The closest of these to the network has a reasonably uniform distribution of $\theta^{B_{\text{in}}}$, and equation (5.2) is satisfied if we take the value of $\overline{\log D}$ to be -1.34. The other two chaotic attractors have non-uniform distributions of $\theta^{B_{\text{in}}}$. We would expect there to be (possibly stable) periodic orbits that visit Y (since $\delta_Y < 1$), but we have been unable to find these. Even if the orbits were stable, we would expect them to have small basins of attraction.

The behaviour observed for parameters in quadrant B of figure 5.1 (for example,

$\delta_X = 0.99$, $\delta_Y = 1.01$) is the same as that seen for quadrant C; since we were unable to locate periodic orbits that visit Y in quadrant C we do not notice their (predicted) absence in quadrant B. The behaviour in quadrants A and D (for example, $\delta_X = 1.01$ and $\delta_Y = 1.01$ or 0.99) is as expected from [18]: the network is attracting, and trajectories that start close enough to the network go towards it, repeatedly and irregularly switching between $+X$ and $-X$, even though in region D, the network is not asymptotically stable (since $\delta_Y < 1$). In both regions, there are stable periodic orbits further away from the network.

6. Resonance bifurcation of a single heteroclinic cycle with complex eigenvalues. To put in context the results we have found for resonance of our Case II network, it is helpful to look at resonance of an isolated cycle in which the linearisation of the vector field has a pair of complex conjugate eigenvalues at one equilibrium of the cycle. The cycle we consider is the same as one of the subcycles of the Case II network with itinerary $A \to B \to X \to A$ except that at equilibrium B there is only a single positive eigenvalue, and hence, the unstable manifolds of all the equilibria in the cycle are one dimensional. Since we are interested in this section in orbits that lie near a single heteroclinic cycle rather than in a continuum of heteroclinic cycles, we can use much simpler forms for the local and global maps than in our analysis of the Case II network, and we are able to compute the full return map with ease; our analysis is analogous to that used for investigation of homoclinic bifurcations of a saddle-focus in, for instance, [14,15]. Furthermore, existence and stability of periodic orbits near the cycle can be deduced from analysis of a single return map; there is no need to look at return maps defined on cross-sections near all the equilibria. We find that at resonance of this cycle an infinite number of periodic orbits appear in saddle-node bifurcations, in a similar way to that seen for resonance in the Case II network.

Specifically, we consider a system of ODEs in $\mathbb{R}^4$ that is equivariant under the symmetries κ_1, κ_2 and κ_3 as defined in (2.1), (2.2) and (2.5), and suppose that there are equilibria, ξ_1, ξ_2 and ξ_3 on the positive x_1, x_2 and x_3 coordinate axes, respectively. These play the role of A, B and X. We assume that there is a connection from ξ_1 to ξ_2 in the invariant (x_1, x_2) plane, a (single) connection from ξ_2 to ξ_3 in the invariant subspace defined by $x_1 = 0$ (this connection is not assumed to lie in a coordinate plane) and a connection from ξ_3 to ξ_1 in the subspace defined by $x_2 = 0$. The existence of invariant hyperplanes allows us to consider just the region of phase space where $x_1 \geq 0$ and $x_2 \geq 0$. To simplify the discussion, we will also consider only trajectories that leave ξ_2 with $x_3 > 0$, that is, we do not consider trajectories that visit $-\xi_3$.

The flow linearised about ξ_1 is given by

$$\dot{u}_1 = -r_1 u_1,\ \dot{x}_2 = e_1 x_2,\ \dot{x}_3 = -c_1 x_3 - \omega y_3,\ \dot{y}_3 = \omega x_3 - c_1 y_3,$$

where r_1, e_1, c_1 and ω are positive constants, and where the u_1 coordinate is obtained

from x_1 after translation to move ξ_1 to the origin of the local coordinate system. Near ξ_2, we use local coordinates u_3 and v_3 that are linear combinations of the global coordinates x_3 and y_3, and local coordinate u_2 that is a translation of x_2. The coordinate x_1 is the usual global coordinate. The flow linearised about ξ_2 is then given by

$$\dot{x}_1 = -c_2 x_1,\ \dot{u}_2 = -r_2 u_2,\ \dot{u}_3 = e_2 u_3,\ \dot{v}_3 = -s_2 v_3,$$

where r_2, e_2, c_2, s_2 are positive constants. The flow linearised around ξ_3 is similar:

$$\dot{x}_1 = e_3 x_1,\ \dot{x}_2 = -c_3 x_2,\ \dot{u}_3 = -r_3 u_3,\ \dot{y}_3 = -s_3 y_3.$$

Here we use a translated u_3 coordinate but the other coordinates are just the global coordinates.

It is convenient to use planar cross-sections near each equilibrium, For instance, we define

$$\mathbf{H}_1^{\rm in} \equiv \{(u_1, x_2, x_3, y_3) \,\big|\, |u_1| < h,\ x_2 = h,\ |x_3| < h,\ |y_3| < h\}$$

and define $\mathbf{H}_2^{\rm in}$, $\mathbf{H}_2^{\rm in}$, $\mathbf{H}_3^{\rm in}$ and $\mathbf{H}_3^{\rm in}$ in a similar and obvious way. We define cross-section $\mathbf{H}_1^{\rm in}$ slightly differently:

$$\mathbf{H}_1^{\rm in} \equiv \{(u_1, x_2, x_3, y_3) \,\big|\, |u_1| < h,\ 0 \le x_2 < h,\ x_0 e^{-\pi c_1/\omega} < x_3 < x_0 e^{\pi c_1/\omega},\ y_3 = 0\}$$

where the positive constant x_0 is chosen so that the heteroclinic connection from ξ_3 to ξ_1 crosses $\mathbf{H}_1^{\rm in}$ at $x_3 = x_0$, and the bounds on x_3 ensure that there is just a single intersection of the connection with the cross-section.

Using these coordinates and cross-sections, it is straightforward to derive local and global maps. To lowest order, these are:

$$\begin{aligned}
\phi_1(u_1,\ x_2,\ x_3,\ 0) &= \left(u_1 \left(\frac{x_2}{h}\right)^{\frac{r_1}{e_1}},\ h,\ x_3 \left(\frac{x_2}{h}\right)^{\frac{c_1}{e_1}} \cos\left(-\frac{\omega}{e_1}\log\left(\frac{x_2}{h}\right)\right),\right. \\
&\qquad \left. x_3 \left(\frac{x_2}{h}\right)^{\frac{c_1}{e_1}} \sin\left(-\frac{\omega}{e_1}\log\left(\frac{x_2}{h}\right)\right)\right), \\
\phi_2(h,\ u_2,\ u_3,\ v_3) &= \left(h\left(\frac{u_3}{h}\right)^{\frac{c_2}{e_2}},\ u_2\left(\frac{u_3}{h}\right)^{\frac{r_2}{e_2}},\ h,\ v_3\left(\frac{u_3}{h}\right)^{-\frac{s_2}{e_2}}\right), \\
\phi_3(x_1,\ h,\ u_3,\ y_3) &= \left(h,\ h\left(\frac{x_1}{h}\right)^{\frac{c_3}{e_3}},\ u_3\left(\frac{x_1}{h}\right)^{\frac{r_3}{e_3}},\ y_3\left(\frac{x_1}{h}\right)^{-\frac{s_3}{e_3}}\right), \\
\Psi_{12}(u_1,\ h,\ x_3,\ y_3) &= (h,\ \epsilon_2,\ ax_3 + by_3,\ cx_3 + dy_3), \\
\Psi_{23}(x_1,\ u_2,\ h,\ v_3) &= (fx_1,\ h,\ \epsilon_3,\ gx_1^2 + ju_2 + kv_3), \\
\Psi_{31}(h,\ x_2,\ u_3,\ y_3) &= (\epsilon_1,\ mx_2,\ x_0 + nu_3 + py_3 + qx_2^2,\ 0),
\end{aligned}$$

where ϵ_i, a, b, c, d, f, g, j, k, m, n, p and q are constants. Composing these maps in order gives the return map $l : \mathbf{H}_1^{\rm in} \to \mathbf{H}_1^{\rm in}$, which to lowest order is:

$$l(u_1,\ x_2,\ x_3,\ 0) = \left(\epsilon_1,\ A_1 x_2^{\delta}\left(x_3 \cos\left(A_2 - \frac{\omega}{e_1}\log x_2\right)\right)^{\frac{c_2 c_3}{e_2 e_3}},\ A_3,\ 0\right), \qquad (6.1)$$

where A_1, A_2 and A_3 are constants and $\delta = (c_1c_2c_3)/(e_1e_2e_3)$. This map is defined for sufficiently small $|u_1|$, x_2 and x_3, with $x_2 > 0$ and $x_3 > 0$. In addition, the map is only defined for values of x_2 for which the cosine is positive.

At lowest order, fixed points of the return map occur for $u_1 = \epsilon_1$, $x_3 = A_3$ and

$$x_2 = Ax_2^\delta \left(\cos\left(A_2 - \frac{\omega}{e_1}\log x_2\right)\right)^{\frac{c_2c_3}{e_2e_3}}, \tag{6.2}$$

where $A = A_1 A_3^{\frac{c_2c_3}{e_2e_3}} > 0$. Equation (6.2) is very similar to the type of fixed point equation obtained in analysis of a Shil'nikov homoclinic bifurcation in a non-symmetric context [14, 15], with the differences being that (6.2) has an exponent on the cosine term and no bifurcation parameter on the left hand side of the equation; this last difference reflects the fact that we are interested in bifurcations that occur as δ varies and the cycle persists but passes through resonance rather than as the cycle is created or destroyed by relative movement of its stable and unstable manifolds.

Figure 6.1 shows schematically graphs of the functions $h_1(x_2) = x_2$ and

$$h_2(x_2) = Ax_2^\delta \left(\cos\left(A_2 - \frac{\omega}{e_1}\log x_2\right)\right)^{\frac{c_2c_3}{e_2e_3}}$$

for qualitatively different choices of δ and A; fixed points of l correspond to intersections of these two graphs. As can be seen in panel (a), if $\delta < 1$ there will exist infinitely many fixed points of the return map, with the fixed points accumulating on the origin. This corresponds to the existence of infinitely many periodic orbits accumulating on the heteroclinic cycle. On the other hand, as shown in panel (b), if $\delta > 1$, there will be no fixed points of the return map in the vicinity of the origin; this corresponds to there being no periodic orbits lying in a sufficiently small neighbourhood of the heteroclinic cycle. The situation for the case $\delta = 1$ depends on the size of A; if $A > 1$ we expect infinitely many periodic orbits to exist when $\delta = 1$, while if $A < 1$ there will be no periodic orbits in a sufficiently small neighbourhood of the heteroclinic cycle when $\delta = 1$.

Consideration of the possible transitions between the different cases shown in figure 6.1 now enables us to sketch schematic bifurcation diagrams showing the behaviour of periodic orbits near the resonance bifurcation. As shown in figure 6.2, in the case that $A > 1$, for sufficiently large $\delta > 1$ there will be no periodic orbits in a small neighbourhood of the heteroclinic cycle. As δ decreases, periodic orbits will be created in pairs in saddle-node bifurcations, with the saddle-node bifurcations accumulating on $\delta < 1$ from above, thus producing an infinite number of periodic orbits for all positive $\delta \leq 1$. For the case $A < 1$, there will similarly be no periodic orbits near the heteroclinic cycle for sufficiently large $\delta > 1$ and infinitely many periodic orbits for $\delta < 1$, but the periodic orbits now appear on the opposite side of the resonance bifurcation; an infinite number of saddle-node bifurcations of periodic orbits accumulate on $\delta = 1$ from below, so an infinite number of periodic orbits will appear all at once as δ decreases through 1.

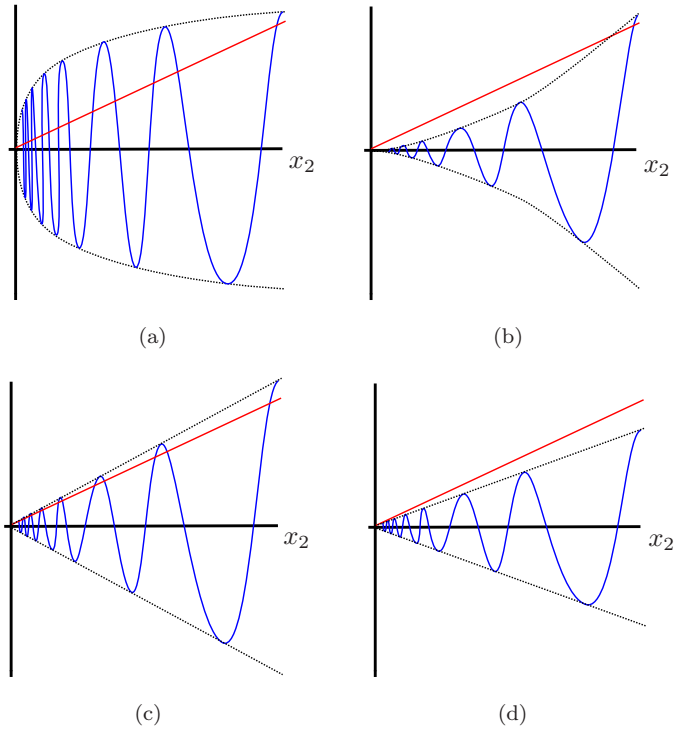

FIG. 6.1. *Schematic diagrams showing the location of fixed points of the return map l, equation (6.1), for different choices of δ and $A = A_1 A_3^{\frac{c_2 c_3}{e_2 e_3}}$. (a) $\delta < 1$; (b) $\delta > 1$; (c) $\delta = 1$, $A > 1$; (d) $\delta = 1$, $A < 1$. Each panel shows the relative position of the graphs of $h_1(x_2) = x_2$ (in red) and $h_2(x_2) = Ax_2^\delta \left(\cos\left(A_2 - \frac{\omega}{e_1}\log x_2\right)\right)^{\frac{c_2 c_3}{e_2 e_3}}$ (in blue). The black dotted curves show the graphs of $h_3(x_2) = \pm Ax_2^\delta$. Fixed points of l correspond to intersections of the graphs of h_1 and h_2. Note that the shape of the graph of h_2 where it cuts the x_2 axis will depend on the exact value of the exponent $\frac{c_2 c_3}{e_2 e_3}$. For the purpose of illustration, we have drawn the case $\frac{c_2 c_3}{e_2 e_3} = 1$, and included $h_2(x_2)$ below the x_2 axis to make the graph easier to read. We are not concerned with values of x_2 for which h_2 is non-positive or undefined.*

Approximate δ values for which saddle-node bifurcations of periodic orbits occur can be computed by comparing the graphs of $h_1(x_2)$ and h_2 plotted in figure 6.1. Specifically, making the approximation that saddle-node bifurcations occur at x_2 values for which h_2 has a local maximum allows us to compute that, to first order, successive saddle-node bifurcations occur at

$$\delta_n = 1 + \frac{\omega \log A}{e_1(2n\pi - A)},$$

from which it follows that the saddle-node bifurcations accumulate on $\delta = 1$ exactly as derived schematically in the previous paragraph. We have not computed the values of δ for which the node-type periodic orbits created in each saddle-node bifurcation are stable, but note that these nodes will likely change stability in period doubling bifurcations near the saddle-node bifurcations, and may undergo cascades of period

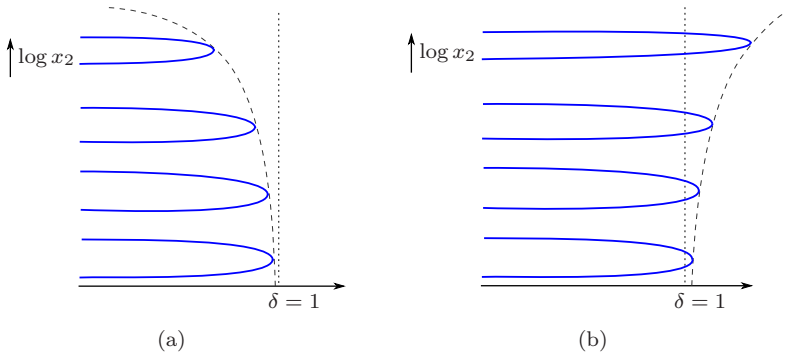

FIG. 6.2. *Schematic bifurcation diagrams for the example of an isolated heteroclinic cycle with complex eigenvalues, showing periodic orbits that occur near the resonance bifurcation at* $\delta = 1$. *(a)* $A < 1$*; (b)* $A > 1$. *Stability of the periodic orbits is not indicated.*

doubling bifurcations leading to chaos, just as occurs in homoclinic bifurcations of saddle-foci [14, 15], and indeed as suggested by the numerical results in section 5.2.5.

The bifurcation diagrams obtained for resonance of this single cycle are completely consistent with the bifurcation diagram for resonance of our Case II heteroclinic network; compare figures 5.14 and 6.2(a). This leads us to conjecture that the appearance of infinitely many periodic orbits near resonance of the Case II cycle is primarily due to the complex eigenvalues in the network not to the network structure. We note, however, two points. First, the analysis in this section explicitly requires that all the equilibria in the network have one-dimensional unstable manifolds and so, while our results are suggestive, they do not apply directly to the network example. Second, our analysis of the Case II network focussed on periodic orbits that made just one circuit of the network before closing and therefore excluded orbits that explored much of the network structure. It is likely that the bifurcation diagram for the network example contains sequences of saddle-node bifurcations additional to those we found. For instance, there might be infinite sequences of bifurcations producing orbits that make one or more visits to Y interspersed with visits to X. Such bifurcations could be regarded as arising from the network structure; investigation of this possibility is left to future work.

7. Discussion. In this article, we have investigated resonance bifurcations in two robust heteroclinic networks; we believe this is the first time any examples of network resonance have been systematically studied. The networks of interest have both previously been studied [17, 18], and consist of a finite number of equilibria connected by heteroclinic connections. An important feature of both networks is that several of the equilibria have two-dimensional unstable manifolds, which results in the existence of an infinite number of heteroclinic cycles in the network, but all the cycles have a common heteroclinic connection. The two networks have the same basic network structure as each other (see figure 1.1) but in one network, one of the

equilibria has a pair complex contracting eigenvalues while in the other network all eigenvalues are real; the equivariance properties of the networks are slightly different to accommodate this feature.

Previous work on these and related networks [1, 2, 4, 16, 18] concentrated on investigating their stability properties and understanding switching dynamics near each network, but did not look in detail at resonance. Here we have focussed on understanding the dynamics resulting from one or more of the heteroclinic cycles in the network undergoing a resonance bifurcation. We have been primarily interested in understanding how much of the observed dynamics can be thought of as arising from resonance of a single cycle and how much is inherently due to the network structure.

Our network with only real eigenvalues (Case I) contains two distinguished heteroclinic cycles, one each in the subspaces defined by $y_3 = 0$ and $x_3 = 0$. We defined δ_X (resp. δ_Y) to be the ratio of contracting to expanding eigenvalues seen by the cycle in the $y_3 = 0$ (resp. $x_3 = 0$) subspace, and investigated the dynamics that occur for δ_X and δ_Y near one. When δ_X or δ_Y passes through one, the corresponding cycle undergoes a resonance bifurcation and, as expected from previous work on such bifurcations [12, 22, 25–27], a periodic orbit appears in the corresponding subspace (see figure 5.8). Within each subspace, there is a transfer of stability between the heteroclinic cycle and the bifurcating periodic orbit, as normally expected for resonance of single cycles. However, because of the network structure, none of the heteroclinic cycles can be asymptotically stable within the full phase space. This observation might lead one to conclude that the bifurcating periodic orbit can never be asymptotically stable, but we show this is not the case; the bifurcating periodic orbit may in some circumstances be asymptotically stable even though the cycle from which it bifurcates is never asymptotically stable.

In addition to the periodic orbits that appear in the subspaces when one or other of the distinguished cycles goes through resonance, there may be further periodic orbits appearing as δ_Y is decreased through one, as shown in figure 5.8(b). These extra periodic orbits are guaranteed to exist if the quantity we called δ_M, which is the maximum ratio of contracting to expanding eigenvalues encountered along any cycle in the network, is greater than one when $\delta_Y = 1$.

Resonance in the network with complex contracting eigenvalues at one equilibrium (Case II) is significantly more complicated than for the case with real eigenvalues. By contrast with Case I, the symmetry properties of this network do not induce the existence of three-dimensional subspaces in which there are distinguished heteroclinic cycles. We can, however, still write down two distinguished combinations of eigenvalues, corresponding to two particular cycles: δ_X (resp. δ_Y) is now the ratio of contracting to expanding eigenvalues seen by the orbit that approaches X (resp. Y) with rate determined by the contracting eigenvalue $c_C(0)$ (resp. $c_C(\frac{\pi}{2})$) as defined in equations (3.10) and (4.8). We investigate the dynamics that occurs for δ_X and δ_Y near one. We find that an infinite sequence of saddle-node bifurcations of periodic

orbits accumulates on each of the lines $\delta_X = 1$ and $\delta_Y = 1$ in the (δ_X, δ_Y) parameter space (see figure 5.14), and expect that there may be period doubling cascades of the orbits created in the saddle-node bifurcations. Note that in the Case II network, the quantity δ_M (as defined above for the Case I network) is again always greater than the maximum of δ_X and δ_Y and thus $\delta_M > 1$ in a neighbourhood of $\delta_X = 1$ and $\delta_Y = 1$. However, δ_M may pass through one in the region where $\delta_X < 1$ and $\delta_Y < 1$. We have shown that the infinitely many periodic orbits created in the resonance bifurcations at $\delta_X = 1$ and $\delta_Y = 1$ will persist so long as $\delta_M > 1$.

In [18], the possibility of chaotic attractors occurring in the Case II network when $\delta_X < 1$, $\delta_Y > 1$ was discussed; here we are able to estimate the location of such an attractor under certain conditions on the spread of orbits. In a numerical example, we found three co-existing chaotic attractors in the regime $\delta_X < 1$, $\delta_Y < 1$. One of these attractors seemed to satisfy the spread condition on orbits, and its location was consistent with our prediction.

Analysis of the dynamics of an isolated heteroclinic cycle with placement of the complex eigenvalues being analogous to the cycles in the Case II network showed (in section 6) the existence of an analogous sequence of saddle-node bifurcations. We thus conjecture that the existence of infinitely many saddle-node bifurcations in the Case II example is due to the presence of the complex eigenvalues rather than arising from the network structure. Note that all equilibria on the isolated cycle analyzed in section 6 had one-dimensional unstable manifolds, and so the results from that example do not carry over directly to our network example, meaning we are unable to make a statement stronger than a conjecture at this stage.

The bifurcations of periodic orbits we have located in our analysis appear to be essentially just those that arise from resonance bifurcations of single heteroclinic cycles, and provide little evidence for the effect of the network structure on the dynamics. However, we have restricted attention to periodic orbits that make just one circuit of the network before closing; it may be that orbits that make two or more circuits of the network (corresponding to orbits of period two or higher in the return maps) are more influenced by the network. One way in which the effect of the network is manifested is in the the role of the quantity δ_M. As discussed in [18] in the context of Case II, network stability is determined by the maximum and minimum ratios of contracting and expanding eigenvalues experienced by any cycle in the network; the network ceases to be asymptotically stable when the minimum ratio (called $\delta^{\min}$ in [18]) decreases through one, and the possibility that orbits not on the stable manifold of an equilibrium of the network might be attracted to the network is erased when the maximum ratio (called δ_M here and $\delta^{\max}$ in [18]) decreases through one. In general, neither the maximum nor minimum ratio is δ_X or δ_Y but is rather some combination of eigenvalues seen on different cycles. In this sense, the important combinations of eigenvalues for resonance of a *network* carry information about the network as a whole, not just about single cycles within the network. We note, however, that in our examples,

because of the geometry of the networks, the minimum ratio of eigenvalues is always either δ_X or δ_Y.

The method of analysis we have adopted in this article is based on the standard procedure for construction of return maps that approximate the dynamics near the network, but with significant adaptations to accommodate the two-dimensional unstable manifolds that occur for some equilibria; elements of the new techniques we have developed were first described by us in [18] but are extended in this article. We believe that similar techniques might be used for the analysis of other heteroclinic networks, and in particular for other networks in which all cycles have a common heteroclinic connection, as is the case in the two networks we considered. Analysis of such networks has, to date, been largely restricted to examining the dynamics near specific cycles in the network, but our techniques enable us to capture the dynamics of the whole network. The issue of extending our techniques to the study of networks in which cycles do not all have a common connection is left for future work.

Finally, we note that numerical work on networks such as those considered here is extremely delicate. The type of analysis we have performed is, as usual, valid in the limit of being close to the network; we have had to look within a distance of 10^{-60} of the network to see some of the phenomena of interest in our numerical examples. On the other hand, very close to our Case II network, the vast majority of orbits visit equilibrium X rather than Y and so it is necessary to wait for a long time before a typical orbit will explore the parts of the network passing near Y. A further complicating factor is that δ_X and δ_Y have to be rather close to one for some phenomena to be observable; otherwise contraction onto or expansion away from the network is too rapid. Thus, while we have located a variety of phenomena by theoretical means, verifying the existence of all these phenomena in particular examples might not be straightforward.

REFERENCES

[1] M. Aguiar, *Is there switching for replicator dynamics and bimatrix games?*, Phys. D, 240 (2011), pp. 1475–1488.

[2] M. Aguiar and S. Castro, *Chaotic switching in a two-person game*, Phys. D, 239 (2010), pp. 1598–1609.

[3] M. A. D. Aguiar, S. B. S. D. Castro and I. S. Labouriau, *Dynamics near a heteroclinic network*, Nonlinearity, 18 (2005), pp. 391–414.

[4] M. Aguiar, I. Labouriau and A. Rodrigues, *Switching near a network of rotating nodes*, Dyn. Syst., 25 (2010), pp. 75–95.

[5] P. Ashwin and M. Field, *Heteroclinic networks in coupled cell systems*, Arch. Ration. Mech. Anal., 148 (1999), pp. 107–143.

[6] P. Ashwin and A. M. Rucklidge, *Cycling chaos: its creation, persistence and loss of stability in a model of nonlinear magnetoconvection,* Phys. D, 122 (1998), pp. 134–154

[7] P. Ashwin, R. Sturman, and A. M. Rucklidge, *Cycling chaotic attractors in two models for dynamics with invariant subspaces,* Chaos, 14 (2004), pp. 571–582.

[8] W. Brannath, *Heteroclinic networks on the tetrahedron,* Nonlinearity, 7 (1994), pp. 1367–1384.

[9] S. B. S. D. Castro, I. S. Labouriau, and O. Podvigina, *A heteroclinic network in mode inter-*

action with symmetry, Dyn. Syst., 25 (2010), pp. 359–396.

[10] T. Chawanya and P. Ashwin, *A minimal system with a depth-two heteroclinic network,* Dyn. Syst., 25, (2010), pp. 397–412.

[11] P. Chossat, M. Krupa, I. Melbourne, and A. Scheel, *Transverse bifurcations of homoclinic cycles*, Phys. D, 100 (1997), pp. 85–100.

[12] R. Driesse and A. J. Homburg, *Resonance bifurcation from homoclinic cycles*, J. Differential Equations, 246 (2009), pp. 2681–705.

[13] R. Driesse and A. J. Homburg, Essentially asymptotically stable homoclinic networks, *Dynamical Systems*, 24 (2009), pp. 459-471.

[14] P. Gaspard, R. Kapral, and G. Nicolis, *Bifurcation phenomena near homoclinic systems: a two-parameter analysis*, J. Stat. Phys., 35 (1984), pp. 697–727.

[15] P. A. Glendinning and C. Sparrow, *Local and global behaviour near homoclinic orbits,* J. Stat. Phys., 35 (1984), pp. 645–696.

[16] A. J. Homburg and J. Knobloch, *Switching homoclinic networks*, Dyn. Syst., 25 (2010), pp. 351–358.

[17] V. Kirk and M. Silber, *A competition between heteroclinic cycles*, Nonlinearity, 7 (1994), pp. 1605–1621.

[18] V. Kirk, E. Lane, C. M. Postlethwaite, A. M. Rucklidge, and M. Silber, *A mechanism for switching near a heteroclinic cycle*, Dyn. Syst., 25 (2010), pp. 323–349.

[19] M. Krupa, Robust heteroclinic cycles, J. Nonlinear Sci., 7 (1997), pp. 129–176.

[20] M. Krupa and I. Melbourne, *Nonasymptotically stable attractors in O(2) mode interactions.* In: Normal Forms and Homoclinic Chaos (W. F. Langford and W. Nagata eds.) Fields Inst., Commun., 4 (1994), AMS, pp. 219–232

[21] M. Krupa and I. Melbourne, *Asymptotic stability of heteroclinic cycles in systems with symmetry*, Ergodic Theory Dynam. Sys. 15 (1995), pp. 121–147.

[22] M. Krupa and I. Melbourne, *Asymptotic stability of heteroclinic cycles in systems with symmetry, II*, Proc. Roy. Soc. Edinburgh Sect. A, 134 (2004), pp. 1177–1197.

[23] I. Melbourne, *An example of a non-asymptotically stable attractor*, Nonlinearity, 4 (1991), pp. 835–844.

[24] C. M. Postlethwaite and J. H. P. Dawes, *Regular and irregular cycling near a heteroclinic network*, Nonlinearity, 18 (2005), pp. 1477–1509.

[25] C. M. Postlethwaite and J. H. P. Dawes, *A codimension two resonant bifurcation from a heteroclinic cycle with complex eigenvalues*, Dyn. Syst., 21 (2006), pp. 313–36.

[26] C. M. Postlethwaite and J. H. P. Dawes, *Resonance bifurcations from robust homoclinic cycles*, Nonlinearity, 23 (2010), pp. 621-642.

[27] A. Scheel and P. Chossat, *Bifurcation d'orbites périodiques à partir d'un cycles homocline symétrique*, C. R. Acad. Sci. Paris, 314 (1992), pp. 49–54.